Journal Pre-proof

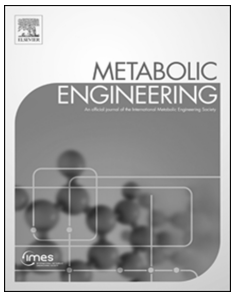

Lipid accumulation in nitrogen and phosphorus-limited yeast is caused by less growth-related dilution

Xi Li, Daniel R. Weilandt, Felix C. Keber, Arjuna M. Subramanian, Shayne R. Loynes, Christopher V. Rao, Yihui Shen, Martin Wühr, Joshua D. Rabinowitz

PII: S1096-7176(25)00129-6

DOI: https://doi.org/10.1016/j.ymben.2025.08.010

Reference: YMBEN 2383

To appear in: *Metabolic Engineering*

Received Date: 7 May 2025

Revised Date: 11 August 2025

Accepted Date: 21 August 2025

Please cite this article as: Li, X., Weilandt, D.R., Keber, F.C., Subramanian, A.M., Loynes, S.R., Rao, C.V., Shen, Y., Wühr, M., Rabinowitz, J.D., Lipid accumulation in nitrogen and phosphorus-limited yeast is caused by less growth-related dilution, *Metabolic Engineering*, https://doi.org/10.1016/j.ymben.2025.08.010.

Lipid accumulation in nitrogen and phosphorus-limited yeast is caused by less growth-related dilution

Xi Li[a,b,h]; Daniel R. Weilandt[a,b,c,h]; Felix C. Keber[b,d]; Arjuna M. Subramanian[a,b]; Shayne R. Loynes[a,b,h]; Christopher V. Rao[e,g]; Yihui Shen[a,b,f]; Martin Wühr[b,d]; Joshua D. Rabinowitz[a,b,c,h,*]

a. Department of Chemistry, Princeton University, Princeton, NJ 08544, United States
b. Lewis Sigler Institute for Integrative Genomics, Princeton University, Princeton, NJ 08544, United States
c. Ludwig Institute for Cancer Research, Princeton Branch, Princeton, NJ 08544, United States
d. Department of Molecular Biology, Princeton University, Princeton, NJ 08544, United States
e. Department of Chemical and Biomolecular Engineering, University of Illinois Urbana-Champaign, Urbana, IL 61801, United States
f. Present address: Department of Bioengineering, University of Pennsylvania, Philadelphia, PA 19104, United States
g. DOE Center for Advanced Bioenergy and Bioproducts Innovation, University of Illinois Urbana-Champaign, Urbana, IL 61801, United States
h. DOE Center for Advanced Bioenergy and Bioproducts Innovation, Princeton University, Princeton, NJ 08544, United States

[*]To whom correspondence may be addressed: Joshua D. Rabinowitz.

Email: joshr@princeton.edu

Author Contributions: X.L., D.R.W.,Y.S., and J.D.R. designed the research. X.L., D.R.W, F.C.K., S.R.L, and A.M.S. performed the research; M.W. supervised the proteomics research; X.L., D.R.W., and F.C.K. analyzed the data; X.L.; D.W.R., F.C.K.,C.V.R., and J.D.R. wrote the paper.

Competing Interest Statement: The authors declared no competing interests.

Abstract

Oleaginous yeasts are used commercially to produce oleochemicals and hold potential also for biodiesel production. In response to nitrogen or phosphorous limitation, oleaginous yeasts accumulate lipids in the form of triacylglycerols. Previous work has investigated potential mechanisms by which nutrient limitation induces lipid biosynthesis without verifying whether lipid biosynthesis flux is actually enhanced. Here we show, using ^{13}C-glucose tracing, that in nitrogen or phosphorous limitation, lipid accumulation occurs without consistent increases in biosynthetic flux. Instead, the main driver of increased lipid pools is decreased growth-related dilution. This conclusion holds across two divergent oleaginous yeasts: *Rhodotorula toruloides* and *Yarrowia lipolytica*. Quantitative proteomics shows a substantial proteome reallocation in response to nitrogen and phosphorous limitation, with ribosomal proteins strongly downregulated, while lipid enzymes are preserved but not consistently upregulated in absolute quantity. Thus, nutrient limitation, rather than triggering greatly enhanced lipid synthesis, results in roughly sustained lipid enzyme levels and biosynthetic flux. Due to slower lipid dilution by cell division, this suffices to drive marked lipid accumulation.

Keywords: *de novo* lipogenesis, oleaginous yeast, isotope tracing, kinetic flux profiling, biodiesel

Main Text

1. Introduction

Microbial cell factories represent a potential sustainable route for producing commodity chemicals and biofuels. Lipids are energy-dense molecules that provide more than twice the caloric content of carbohydrates per gram, making them an efficient means for energy storage (Nelson and Cox, n.d.). Triacylglycerols (triglycerides) are the major form of storage lipids and immediate precursors to biodiesel, which is needed industrially in large quantities to power commercial shipping and other aspects of a renewable economy. Oleaginous yeasts such as *Rhodotorula toruloides* and *Yarrowia lipolytica* naturally accumulate triglycerides under nutrient limitation (especially nitrogen limitation) and can be further engineered to enhance triglyceride synthesis (Blazeck et al., 2014; Coradetti et al., 2018a; Park and Ledesma-Amaro, 2023; Qiao et al., 2017; Ratledge, 2010; Wang et al., 2018).

The oleaginous yeasts *Y. lipolytica* and *R. toruloides* diverged approximately 450 - 600 million years ago, early in the evolution of fungi (Lücking et al., 2009; Shen et al., 2016; Taylor and and Berbee, 2006; Yang et al., 2012). While less studied than Baker's yeast, *Y. lipolytica* has emerged as an increasingly important organism for both pure and applied research, due to its genetic tractability, metabolic versatility, and industrial utility in producing lipids, such as eicosapentaenoic

acid (EPA), a vegetarian omega-3 supplement (Park and Ledesma-Amaro, 2023; Qin et al., 2023; Xie et al., 2015). Transcriptomic analyses of *Y. lipolytica's* transition into nitrogen limitation revealed that lipid accumulation occurs with extensive global transcriptional reorganization but relatively modest changes to lipogenic gene expression (Morin et al., 2011). Flux modeling supported rewiring of amino acid metabolism to direct carbon towards fat (Kerkhoven et al., 2016).

R. toruloides is substantially less extensively studied than *Y. lipolytica,* but has appealing qualities for a potential future industrial lipid producer, including the native capacity to utilize diverse carbon substrates present in lignocellulosic biomass (Hu et al., 2009; Saini et al., 2020; Chmielarz et al., 2021; Dias et al., 2023; Jagtap et al., 2021; Tiukova et al., 2019). Multiomics analysis of *R. toruloides* under phosphorus limitation showed that lipid accumulation is accompanied by the downregulation of ribosomal genes and upregulation of lipogenic genes (Wang et al., 2018). Lipidomic analysis of *R. toruloides* under varying degrees of nitrogen limitation showed that di- and triacylglycerols accumulate at the expense of phospholipids. Transcriptomics of *R. toruloides* under the same conditions revealed downregulation of ribosomal and amino acid synthesis genes with upregulation of lipid synthesis genes transcripts (Mishra et al., 2024). Overall, these studies aim to understand how lipids accumulate in response to nitrogen and phosphorus limitation. They conclude that either an upregulation of genes involved in lipid synthesis or a downregulation of competing metabolic pathways is responsible for driving lipid accumulation. Notably, however, none of the studies directly demonstrate that lipid synthesis flux increases. Instead, they assume that increased lipid content arises primarily from increased synthesis.

One important method for quantifying cellular metabolic flux is metabolic flux analysis (MFA). In classical MFA, stoichiometric constraints from the metabolic network architecture, biomass accumulation rates, and steady-state ^{13}C-labeling data are integrated within a flux-balanced computational model (Antoniewicz, 2021; Gopalakrishnan and Maranas, 2015; Martín et al., 2015; Sauer, 2006). This approach is both experimentally and computationally efficient (only steady-state measurements and algebraic calculations are required). A limitation is that the steady-state tracing data are only informative regarding convergence points in metabolism (i.e. where branches reconnect, like upper glycolysis and the pentose phosphate pathway rejoining at glyceraldehyde-3-phosphate). Biosynthetic fluxes are not measured, only inferred based on biomass composition and growth rate, which ignores the potential for simultaneous biomass synthesis and catabolism. For measuring biosynthetic fluxes, dynamic isotope tracing is required, with the initial pre-steady-state rate of labeled product accumulation proportional to biosynthetic flux (Jang et al., 2018).

In this study, we quantify lipid synthetic fluxes based on the kinetics of fat labeling from ^{13}C-glucose tracer. Under nitrogen or phosphorous limitation, lipid accumulation occurs without corresponding increases in fatty-acid synthesis flux. Instead, the main driver of increased lipid pools is decreased growth-related dilution. Proteomics data align in showing that lipid biosynthetic enzymes are preserved but not strongly upregulated in absolute quantity during nutrient limitation.

Thus, nutrient limitation results in sustained lipid synthesis in the face of slower lipid dilution by cell division, which suffices to drive marked lipid accumulation.

2. Materials and Methods

2.1 Media

For nutrient-replete condition, also referred to as the control, yeasts were grown in minimal media containing 6.7 g/L yeast nitrogen base without amino acids (YNB (-) AA, Sigma, Y0626) and 20g/L glucose. For nutrient-limited conditions, YNB without amino acids or ammonium or phosphate (YNB (-) AA (-) NH_4 (-) PO_4, MP Biomedicals 114029622) was used as the mineral base and was supplemented with nutrients specified in Table S1 (adapted from Shen et al., 2024). Except where otherwise indicated, the starting glucose concentration in the nutrient-replete condition was set higher than in the nutrient-limited conditions (20 g/L vs. 5 g/L) to prevent glucose depletion during growth. For nitrogen limitation, we initially tested an ammonium sulfate concentration of 0.05 g/L (C/N molar ratio of 220) for both yeasts based on literature data for *R. toruloides* (Boer et al., 2010; Zhu et al., 2012*)* but changed to 0.1 g/L for *Y. lipolytica* as the initial lower concentration resulted in premature growth termination as opposed to nutrient-limited growth. All media were prepared from Milli-Q water, filtered sterilized through 0.22 µm pore filter.

2.2 Strains and culture

The *R. toruloides* strain (IFO0880) used in this study was isolated from cultures collected by the National Institute of Technology and Evaluation (NBRC), Japan. The *Y. lipolytica* strain (W29) was isolated from wastewater in Paris (Barth and Gaillardin, 1996).

Cell density was quantified by OD at 600 nm (OD_{600}) as measured by a UV-Vis spectrophotometer (GENESYS 10, Thermo) with tenfold dilution by water. The yeasts were first precultured overnight in either in nutrient-replete or nutrient-limited media (to match the desired growth condition). Then the yeast cells were pelleted (590 $\times$ g for 2 min at room temperature) and washed before inoculation into fresh medium with a starting OD_{600} of 0.05. The cultures were performed in 150-ml vented baffled culture flasks (Wasylenko et al., 2015) with 15 - 20 ml of medium, in a shaker at 30°C, 250 rpm. For nutrient-replete conditions, yeast cultures were harvested for isotope tracing or proteomics analysis at an OD_{600} of around 0.6 for *R. toruloides* and 1.0 for *Y. lipolytica*. For nutrient-limited conditions, cells were allowed to grow just long enough to trigger the lipid accumulation phenotype but were harvested before reaching the stationary phase. Specifically, *R. toruloides* cultures were harvested at OD_{600} around 0.75 under nitrogen limitation and around 1.0 under phosphorus limitation, while *Y. lipolytica* cultures were harvested at OD_{600} around 0.9 and around 1.2 under nitrogen and phosphorus limitation, respectively.

2.3 Fatty acid saponification and biomass hydrolysis

Fatty acids from biomass were subjected to alkaline saponification (Zhang et al., 2017). Cells equivalent to 1 OD·ml were pelleted and washed twice with ice cold water. The pellets were then transferred to a 4 ml glass vial (with PTEF-lined polypropylene caps, to reduce background saturated fatty acids from plastic labware) with 1 ml 0.3 M KOH in 90:10 methanol: water. The samples were placed in 80 °C water bath for 1 hour, cooled down, and neutralized with 100 µl formic acid. 1 ml hexane was used to extract fatty acids from the aqueous phase, and then the extracts were transferred to glass vials and dried under nitrogen flow. The dried extracts were redissolved in 200 μL of 50:50 acetonitrile: methanol solution for LC-MS analysis.

Acid hydrolysis was performed to detect the monomers of protein, DNA, RNA, or carbohydrate from yeast biomass. Yeast cells equivalent to 1 OD·ml were pelleted, washed twice with cold ice water, and then hydrolyzed for 2 hours in 100 µl of 6M HCl at 80 °C and 300 rpm with a thermomixer. The hydrolysate was centrifuged, and 10 µl of supernatant was dried under nitrogen gas and redissolved in 80 µl of 40:40:20 acetonitrile:methanol:water for LC–MS analysis.

2.4 Biomass pool size and composition quantification

For quantification of lipid in biomass, yeast cells equivalent to 1 ml of OD_{600} = 1 were saponified in 1 ml saponification solvent with internal standards of 20µM [U-$^{13}C_{16}$] palmitate, 20µM [U-$^{13}C_{18}$] oleate, and 20µM [U-$^{13}C_{18}$] linoleate. The concentrations (C_i) of fatty acids with an internal standard were then quantified by scaling the ratio of the ^{12}C and ^{13}C ion counts with the standard concentration:

$$C_i = 20\mu\text{M}\frac{TIC_{C12,i}}{TIC_{13,i}}$$

where $TIC_{C12,i}$ and $TIC_{C13,i}$are the total ion counts from cells and the three fully labeled standards respectively. The remaining fatty acid concentrations (C_j) were quantified by scaling the ratio between their respective ^{12}C ion count and the ^{13}C signal averaged across the three fully labeled internal standards with the standard concentration:

$$\langle TIC_{C13,F}\rangle = \frac{1}{3}\sum_{i=1}^{3} TIC_{13,i}$$

$$C_j = 20\mu\text{M}\frac{TIC_{C12\ j}}{\langle TIC_{C13,F}\rangle}$$

where $TIC_{C12,j}$ are the total ion counts of fatty acid species that do not correspond to any of the internal standards.

The protein, DNA, RNA, and carbohydrate pool sizes were measured by using ^{13}C labeled *Saccharomyces cerevisiae* cultured under carbon limitation with [U-$^{13}C_6$]glucose at 0.1 h^{-1} as an internal standard (Shen et al., 2024). Yeast cells corresponding to 1 ml of OD_{600} = 1 from each sample were mixed with an equal amount of the fully ^{13}C labeled *S. cerevisiae* and subjected to

acid hydrolysis. The $^{12}C/^{13}C$ ratios of the detected hydrolysis products (amino acids, deoxyribonucleic acids, ribonucleic acids, and saccharides) from different biomass component (protein, DNA, RNA, and carbohydrate) were multiplied by the known abundance of hydrolysis products in the labeled standards. Summing these values yielded the abundance of each biomass component *b* (C_b) in the sample cells:

$$C_b = \sum_{i}^{N} \frac{TIC_{C12,i}}{TIC_{13,i}} C_{b,i}^{S.C.}$$

where $TIC_{C12,i}$ and $TIC_{C13,i}$ are the total ion counts of the *N* measured hydrolysis product of a biomass component *b* from the sample cells and fully labeled yeast standard, respectively, and $C_{b,i}^{S.C.}$ is the known abundance of the corresponding hydrolysis product of biomass in *S. cerevisiae*.

The final biomass pool sizes of lipid, protein, carbohydrate, DNA, and RNA were obtained by normalizing each of the biomass component concentrations by their total sum:

$$X_b = \frac{C_b}{\sum_l^5 C_l}$$

where X_b are the pool sizes of the five biomass components in units of g/gDCW.

2.5 ^{13}C isotope tracing experiments

[U-$^{13}C_6$]glucose was used to quantify biomass flux in growing cells. The yeasts were grown in unlabeled media (without tracer) until OD_{600} was between 0.6 – 1. Yeast cells were then pelleted and inoculated into fresh media (without tracer) at a starting OD_{600} around 0.2 and allowed to grow until OD_{600} reached for *R. toruloides* around 0.4 for the nutrient-replete condition and 0.7 for the nutrient-limited conditions, and for *Y. lipolytica* around 0.7 for the nutrient-replete condition and the 1.0 for nutrient-limited conditions. A solution containing 200g/L [U-^{13}C]glucose was then spiked into the culture containing 5 g/L glucose at a 1/120 v/v ratio, resulting in a final glucose concentration of 6.67g/L, comprising 1.67g/L [U-^{13}C]glucose, a glucose enrichment of 25%. Similarly, in culture with starting glucose as 20g/L, 200 g/L [U-^{13}C]glucose was spiked in at a 1/30 v/v ratio, resulting in a final glucose concentration of 25.8 g/L, comprising 6.45 g/L [U-^{13}C]glucose, again 25% enrichment. We then collected samples at 20 minutes, 50 minutes, 80 minutes, and 110 minutes. For lipid synthesis measurements, fatty acids were saponified, and for protein synthesis measurements, proteins were subjected to acid hydrolysis. The resulting samples were analyzed by liquid chromatography-mass spectrometry (LC-MS) to determine the ^{13}C-mass isotopologue distribution in fatty acids and amino acids from the biomass component. For saturated fatty acid labeling analysis, raw results were background-corrected by subtracting the values from a procedure blank to account for contamination from saturated fatty acids. Assuming that the yeasts are at approximate metabolic steady state but not isotopic steady state during the labeling duration (i.e. stable metabolite pool sizes and fluxes, but increasing labeling), the flux to lipid and protein in biomass was calculated from the labeling kinetics of the fatty acids/amino acids into whole-cell lipids and protein and biomass pool size.

2.6 Lipid synthesis flux calculation

The lipid synthesis flux was computed using the fraction of newly synthesized fat (*D*). In the simplest case where the experimentally measured mass isotopologue distribution (MID) of fatty acid (Argus et al., 2018; Hellerstein and Neese, 1992; Kelleher and Masterson, 1992; Tumanov et al., 2015; Zhang et al., 2021, 2017) after natural isotope correction results solely from the condensation of two carbon units, the evenly labeled fractions of the newly synthesized fatty acid follow a binomial distribution:

$$f_{2n} = D\binom{N}{n}L^n(1-L)^{N-n}$$

where f_{2n} is the fraction of the fatty acid with 2*n* ^{13}C-labeled carbon atoms (i.e. of mass M+2*n*), *D* is the fraction of fatty acid that was newly synthesized during the labeling duration, N is the number of two carbon units per fatty acid (i.e. *N* = 8 for palmitate), *L* is the *M*+2 fraction of acetyl-CoA and *n* is an integer smaller equal *N*. The unlabeled mass isotopologue fraction additionally accounts for the amount of old fat:

$$f_0 = (1-D) + (1-L)^N$$

In practice, there is also a small amount of M+1 acetyl-CoA arising from scrambling reactions in central metabolism, and hence the actual data also contains odd-labeled forms and accordingly was fitted to the trinomial analogue of the above equations. The amount of unlabeled, *M+1* (minor) and *M*+2 labeled acetyl-CoA ($\vec{L}$ = *[M+0, M+1, M+2]*) and the fraction of newly synthesized fat (scalar *D*) was quantified by fitting the experimentally determined fatty acid labeling to the theoretical distribution for each timepoint and minimizing the sum of squared residuals SSR using constrained nonlinear optimization, ensuring that the acetyl-CoA M+0, M+1, and M+2 fractions are all non-negative and sum to one:

$$\mathrm{MID}_{sim}^{n} = D \cdot \mathrm{MID}_{sim}^{(n-1)} * \vec{L} + (1-D)\,[1,0,0,\ldots,0]^T$$

$$SSR = \sum_{i}^{N}\left(\mathrm{MID}_{sim,i}^{N} - \mathrm{MID}_{exp,i}^{N}\right)$$

where MID_{sim}^{n} is the simulated and MID_{exp}^{n} the experimentally determined labeling distribution of the acyl chain of length *n*, the $*$ operator denotes convolution of two vectors as previously defined(Zhang et al., 2021, 2017).

To determine the lipid flux, the relative labeling rate (k) was determined by fitting the time-dependent newly synthesized palmitate (D) to a single exponential production curve (Lee et al., 2025; Yuan et al., 2008, 2006):

$$D(t) = 1 - \exp(-kt)$$

The lipid flux is calculated by multiplying the relative labeling rate for palmitate by the total lipid pool size:

$$v_{lipid} = k \cdot X_{lipid}$$

where v_{lipid} is the lipid synthesis flux, X_{lipid} is the total amount of saponified fatty acids per in units of g/gDCW. Alternatively, v_{lipid} can be calculated by applying the same approach for each of palmitate, oleate, and linoleate, with the contribution of each weighted by their measured relative abundance.

A further complication to the above approach is that lipid labeling can be delayed by the time required to convert fatty acid intermediates and to end products. The above equations assume that such delays are negligible. This assumption is supported by dynamical simulations that include also fatty acid biosynthetic intermediates and by comparison of these simulations with the experimental labeling data (see Supplementary Note).

2.7 Protein synthesis flux calculation

Similar to lipid flux measurement, the normalized labeling of amino acids (a.a.) ($L_{a.a.}$) was determined by directly normalizing the labeled fraction of carbon atoms in the amino acid (F) by the glucose enrichment (E), i.e., the relative amount of fully labeled glucose in the media.

$$L_{a.a.} = F/E$$

where the labeled fraction of carbon atoms is calculated as

$$F = \frac{\sum_{i=0}^{n} i\, f_i}{n}$$

with f_i as the fraction of mass isomers with *i* being labeled carbons for a molecule with n number of carbons. The relative labeling rate (k) was determined by fitting the time dependent labeling (L) of three amino acids (valine, serine, and alanine) to an exponential of the form (Lee et al., 2025; Yuan et al., 2008, 2006):

$$L_{a.a.}(t) = 1 - \exp(-kt)$$

The labeling rates were then averaged across the three amino acids to obtain a $\bar{k}$. The protein flux is calculated by multiplying the averaged relative labeling rate with the protein pool size:

$$v_{protein} = \bar{k} \cdot X_{protein}$$

where $v_{protein}$ is the protein synthesis flux, $X_{protein}$ is the pool size of the protein in units of g/gDCW.

2.8 Metabolomics analysis by liquid chromatography-mass spectrometry

Saponified fatty acids were analyzed on the Q Exactive Plus hybrid quadrupole-orbitrap mass spectrometer (Thermo Scientific). LC separation was done by a reversed-phase method through an Agilent InfinityLab Poroshell 120 EC-C18 column (2.1× 150 mm, 2.7-µm particle size, 120 Å pore size, 693775-902), where solvent A was 90:10 water: methanol with 1 mM ammonium acetate and 0.2% (v/v) acetic acid (pH 3) and solvent B was 98:2 isopropanol: methanol with 1 mM ammonium acetate and 0.2% (v/v) acetic acid (pH 4.5). The column temperature was set at 60 ℃, the flow rate was 0.15 ml/min, and the injection volume was 3µL. The LC gradient was: 0 min 25%

B; 2 min 25% B; 4 min 65% B; 16 min 100% B; 20 min 100% B; 21 min 25% B; 25 min 25% B, stop run. MS full scans were in negative ion mode with an orbitrap resolution of 70,000 and scan range of m/z 220-600. The AGC target was 3e6, and the maximum injection time was 300ms.

Separation for polar metabolites such as amino acids, nucleotides, and sugars was achieved by hydrophilic interaction liquid chromatography (HILIC) with an XBridge BEH amide column (2.1 mm × 150 mm, 2.5 µm particle size; Waters, 186006724). The column temperature was set at 25°C. Solvent A was 95 vol% H_2O 5 vol% acetonitrile (with 20 mM ammonium acetate, 20 mM ammonium hydroxide, pH 9.4). Solvent B was acetonitrile. Flow rate was 0.15 mL/min. The LC gradient was: 0-2min, 90% B; 3-7min, 75% B; 8–9 min, 70% B; 10–12 min, 50% B; 12–14 min, 25% B; 16–20.5 min, 0.5% B; 21–25 min, 90%. MS analysis was performed on Thermo Fisher's Q Exactive Plus (QE+) Hybrid Quadrupole-Orbitrap, Orbitrap Exploris 240 or 480 mass spectrometer. Full scan was performed in negative mode, at the m/z of 70–1000. The automatic gain control (AGC) target was 3e6 on QE+ and 1000% on Exploris 240/480. The maximum injection time was 500 ms. The orbitrap resolution was 140,000 on QE+, and 180,000 on Exploris 240/480.

Raw mass spectrometry data collected with XCalibar (Thermo Scientific) were converted to .mzXML format by ProteoWizard (https://proteowizard.sourceforge.io). Unlabeled parent signals of fatty acids/amino acids and their corresponding isotopologues were quantitated on El Maven (V0.12.1-beta). Natural isotope abundance was corrected by the AccuCor(Su et al., 2017) package (https://github.com/lparsons/accucor) on R or 'Isocorr' package (https://github.com/MetaSys-LISBP/IsoCor) on MATLAB.

2.9 Proteomics sample preparation

Yeast proteomics sample preparation followed a typical workflow (Gupta et al., 2018). Yeast cells equivalent to 20 ml of OD_{600} = 1 were pelleted (2800 ×g for 5 mins at 4°C), rapidly frozen in liquid nitrogen before grounded by CryoMill (Retsch) at 25 Hz for 5-10 min. The powder was lysed in 50 mM HEPES (pH 7.2), 4% SDS and 1mM dithiothreitol at 95 °C and 1400 rpm with a thermomixer. The final supernatant in the lysate contained 1-2 mg/ml protein, determined by a reducing agent-compatible Bicinchoninic Acid Assay (Pierce BCA Protein Assay Kit, Thermo Scientific). To reduce disulfide bonds, dithiothreitol (DTT) was added to a final concentration of 5 mM and incubated for 20 minutes at 60°C. After cooling to room temperature, cysteines were alkylated with N-ethyl maleimide (NEM) at a final concentration of 20 mM for 20 minutes at room temperature, and NEM was subsequently quenched by an excess of 10 mM DTT.

For relative protein quantification samples, proteins were purified by SP3 precipitation onto magnetic beads (SpeedBead Magnetic Carboxylate, Cytiva) in 50% ethanol, then washed three times with 80% ethanol using a KingFisher robot (Thermo)(Hughes et al., 2019). Protein digestion was performed overnight with 20 ng/µL LysC (Wako) in 2 M guanidine hydrochloride and 10 mM EPPS (pH 8.5) with agitation at 24°C. The reaction was then diluted fourfold with 10 mM EPPS,

and an additional 20 ng/µL LysC and 10 ng/µL trypsin (Promega) were added; incubation continued overnight at 37°C. Samples were vacuum-dried and resuspended in 200 mM EPPS (pH 8.0) to achieve a peptide concentration of 1 µg/µL. Each sample was labeled with TMTpro (Thermo Scientific) tags for 2 hours at room temperature at a 5:1 mass ratio of TMTpro to peptide, then quenched with 0.5% hydroxylamine for 30 minutes at room temperature before combining different conditions. The samples were dried, resuspended in 100 µL of HPLC water, acidified to pH < 2 with HPLC-grade phosphoric acid, and desalted using C18 stage tips (Pierce) (Rappsilber et al., 2007).

For absolute quantification samples, proteins were precipitated by methanol-chloroform and resuspended in 6 M guanidine hydrochloride. The Proteomics Dynamic Range Standard (UPS2; Sigma-Aldrich) was spiked into the lysate at a 1:300 ratio by protein mass, and proteins were digested as described above. Samples were acidified (to pH < 2) with phosphoric acid and clarified by ultracentrifugation. The supernatants were dried using a vacuum evaporator at room temperature. After resuspension, the samples were sonicated for 5 minutes and fractionated by medium pH reverse-phase HPLC (Zorbax 300Extend C18, 4.6 x 250 mm column, Agilent). The 96 elutions were pooled into 24 fractions by alternating wells in the plate (Edwards and Haas, 2016). Each fraction was dried, resuspended, acidified, and processed as described above.

2.10 Peptide analysis by liquid chromatography–mass spectrometry

Approximately 1-3 µg of each sample/fraction in 1% formic acid was analyzed by LC-MS. The fractionated samples for absolute quantification were analyzed using a label-free data-dependent acquisition method on an nLC-1200 HPLC (Thermo Fisher Scientific) coupled to an Orbitrap Fusion Lumos (Thermo Fisher Scientific), using a custom made C18 LC-column. The multiplexed sample was analyzed using a Real-Time-Search MS3 method(McAlister et al., 2014; Schweppe et al., 2020) on a Neo Vanquish (Thermo Fisher Scientific) coupled to an Orbitrap Ascend (Thermo Fisher Scientific) using an Aurora Series emitter column (25 cm x 75 µm ID, 1.6 µm C18) (ionopticks, Australia). Columns were held at 60°C during separation by an in-house built column oven. Separation was achieved by applying a 12% to 35% acetonitrile gradient in 0.125% formic acid and 2% DMSO over 90 min at 350 nL/min at 60°C. Electrospray ionization was enabled by applying a voltage of 2.6 kV at the inlet of the microcapillary column.

2.11 Proteomics data analysis

Mass spectrometry data analysis was performed essentially as previously described (Sonnett et al., 2018). The mass spectrometry data in the Thermo RAW format was analyzed using the Gygi Lab software platform (GFY Core Version 3.8) licensed through Harvard University. Peptides that matched multiple proteins were assigned to the proteins with the greatest number of unique peptides.

For relative quantification of TMT-tagged samples the area of TMT reporter ion belonging to each protein was summed up. The signal was normalized to the mean across samples and then median normalized within each sample.

For absolute protein abundances in label-free samples, for each protein, area of precursor ion intensity (I) from all peptides was summed and normalized by the number of theoretical peptides. Signals from UPS2 proteins were used to construct a calibration curve, which was then fitted to a power law to obtain the absolute concentration of yeast proteins:

$$\ln(I) = k \ln(C) + A$$

where C is the protein concentration, and k, A are fitting parameters. The log-linear coefficient k is 0.97 and 0.85 for *R. toruloides* and *Y. lipolytica,* respectively. In each yeast strain, the absolute protein abundance is reported as mass fraction in the whole proteome, which was approximated by the product of molar concentration and amino acid sequence length normalized to the sum of all proteins. Absolute protein abundance under nutrient limitation conditions was inferred from the relative fold change to batch culture obtained with relative quantification.

In each yeast strain, metabolic enzymes were initially identified and mapped to specific pathways using the respective genome-scale model *iYali4* (Kerkhoven et al., 2016) for *Y. lipolytica* and *iRhto1108* (Dinh et al., 2019) for *R. toruloides*. All enzymes were then assigned to functional sectors based on the subsystem annotated in the genome scale model. Proteins that could not be annotated using the genome scale model were classified into functional sectors based on the UniProt reference proteome annotations from (UP000001300 for *Y. lipolytica* and UP000199069 for *R. toruloides*). To align the proteome annotation of the *R. toruloides* genome scale model (which is based on the *R. toruloides* strain NBRC 0880) and the UniPort reference proteome for *R. toruloides* we performed a BLASTp alignment.

The complete list of functional assignments and the individual protein abundances (normalized to whole proteome), along with python code to generate the pathway assignments can be found on github (https://github.com/Xili-hope/Rhoto_Yarli_DNL_regulation). The mass spectrometry proteomics data have been deposited to the ProteomeXchange Consortium via the PRIDE (Perez-Riverol et al., 2019) partner repository with the dataset identifier PXD PXD063019 and 10.6019/PXD063019.

3. Results

3.1 R. toruloides and Y. lipolytica accumulate lipids upon nitrogen or phosphorus limitation.

We used a simple batch culture system (shake flasks) to induce nitrogen or phosphorus limitation for both *R. toruloides* and *Y. lipolytica* (Fig. 1A). As expected, both yeast species exhibited slower growth under nutrient-limited conditions (Fig. 1B-F). Measurement of biomass composition (Fig. 1D,G) revealed that the nutrient limitation induced increased lipid biomass fraction at the

expense of less protein and nucleic-acid biomass fraction (especially for nitrogen limitation) and sometimes also less carbohydrate biomass fraction (for *R. toruloides* phosphate limitation). Quantitatively, lipids accumulated by 3 - 5 fold upon nutrient limitation, with the greatest accumulation (nearly 50% of biomass) in nitrogen-limited *R. toruloides.*

3.2 Isotope tracing shows sustained lipogenic flux

We next set out to assess whether the observed lipid accumulation induced by nitrogen and phosphate limitation was driven by increased fatty acid flux. To measure flux, we monitored the kinetics of stable isotope-labeled carbon from glucose into whole-cell fatty acids (free, membrane lipids, and lipid droplets, based on saponification of whole cell lipids; Fig. 2A). Specifically, cells were cultured in nutrient-replete (control) or nutrient-limited conditions (Fig. S1). Then [U-$^{13}C_6$]glucose was added to cells to increase the total glucose abundance by 33% (such that 25% v/v of the total glucose was labeled), and the cells were allowed to grow for varying durations, after which they were quickly harvested by centrifugation. Then, fatty acids were saponified from total cellular lipids by alkaline hydrolysis, and the fractional labeling of fatty acids was measured by liquid chromatography-mass spectrometry (LC-MS). Since glucose is not fully labeled, fatty acid labeling was normalized to the labeling of its precursor, acetyl-CoA. Instead of directly measuring acetyl-CoA, its labeling fraction was inferred by fitting the measured fatty-acid mass isotopologue distribution (Fig. S2A,C), based on the fraction of newly synthesized fatty acids and the binomial condensation of labeled and unlabeled acetyl-CoA units (Argus et al., 2018; Hellerstein and Neese, 1992; Kelleher and Masterson, 1992; Tumanov et al., 2015; Zhang et al., 2021, 2017). We found across different conditions, after adding the labeled glucose, the M+2 fraction of acetyl-CoA increased quickly to about 20%, somewhat less than the fractional glucose labeling, reflecting modest other inputs to acetyl-CoA, such as fatty-acid recycling (Fig. S2D,H). The fraction of newly synthesized fatty acids increased more slowly, reflecting incorporation of glucose carbons into triglycerides, i.e., lipogenic flux.

Assuming first-order kinetics, fatty acid labeling increases with time in a single exponential manner, with the exponential time constant equal to the biosynthetic flux divided by the fat pool size (Yuan et al., 2006). Accordingly, high flux tends to lead to fast labeling. Surprisingly, compared to nutrient-replete growth, in both yeasts, the fraction of newly synthesized palmitate (C16:0), the direct product of *de novo* fatty acid synthesis, rises more slowly, rather than quickly, in nitrogen or phosphorus limitation (Fig. 2C,F). In nutrient-replete conditions, labeling kinetics were indistinguishable across high glucose (20 g/L) and lower (but not limiting) glucose (5 g/L) (Fig. S3). Thus, relative to the total fat pool size, flux is slower rather than faster in the nitrogen- or phosphate-limited yeast.

To convert labeling kinetics into absolute biosynthetic fluxes, it is necessary to multiply the exponential time constant of the labeling curve by the size of the total pool being labeled. Multiplying

the total fatty-acid pools by the rate constant calculated based on newly synthesized palmitate fraction reveals that overall fatty acid biosynthetic flux is unaffected by high versus lower (but not limiting) glucose in nutrient-replete conditions (Fig. S3). Crucially, fatty acid biosynthetic flux remains nearly unchanged under nitrogen limitation and subtly increased under phosphorus limitation in R. *toruloides.* Specifically, absolute lipogenic flux increased by 40% under phosphorus limitation and showed minimal change under nitrogen limitation (Fig. 2D), while fat pool size increased by 250 – 460% (Fig. 2B). In *Y. lipolytica,* flux remained largely unchanged under both nitrogen and phosphorus limitation (Fig. 2G), despite a 220% - 240% increase in lipid pool size in each condition (Fig 2.E).

For simplicity, these analyses were based on the labeling kinetics of palmitate. While palmitate is one of the most abundant fatty acids, a majority of fatty-acid biomass is in the form of longer fatty acids (Fig. S4). The same pattern of labeling kinetics, however, was observed across different fatty-acid species (Fig. 3, Fig. S5 A-C, E-G), which are produced from palmitate (Argus et al., 2018; Wakil, 1989). Further, to confirm the robustness of our results, we also estimated lipid biosynthetic flux by incorporating palmitate, oleate (C18:1), and linoleate (C18:2), which together account for 60% - 80% of total lipid mass. The weighted average flux based on their relative abundance showed the same trend: flux remained similar under nitrogen limitation and modestly increased under phosphorus limitation (by 60%, Fig. S5 D,H). Thus, unlike the consistently increased lipid pool size, lipid biosynthetic flux does not change consistently with nutrient limitation. Notably, in all examined cases, the extent of lipid flux increase induced by nutrient limitation is insufficient to account for the increase in lipid pool size. Accordingly, pool size must also be increased due to decreased outflow or dilution. This led us to the concept that lipid accumulation during nutrient limitation results from sustained synthesis with decreased dilution by growth.

3.3 Proteomics reveals sustained lipid biosynthetic enzyme abundances

Next, we analyzed protein abundance and overall proteome composition for *R. toruloides* and *Y. lipolytica,* cultured as described above (Fig. 1A). Using LC-MS/MS proteomics, we quantified the abundance of approximately 2,500 proteins in each yeast species, and each protein was allocated into a functional sector, e.g., translation, lipid synthesis, energy metabolism (Fig. 4; Fig. S6).

Ribosomal protein mass fraction decreased in both *R. toruloides* and *Y. lipolytica* under nitrogen and phosphorus limitation (Fig. 4 A,E). This aligns with previous findings that faster growth rates correlate with higher ribosomal fractions, including in *R. toruloides* and *Y. lipolytica* (Coradetti et al., 2018b; Kerkhoven et al., 2016; Metzl-Raz et al., 2017; Poorinmohammad et al., 2022; Schaechter et al., 1958; Scott et al., 2014; Shen et al., 2024; Xia et al., 2022; Zhu et al., 2012), and that total RNA content, largely comprising ribosomal RNA, decreases as growth slows (Fig. 1D,G).

In contrast, the total mass fraction of metabolic proteins remained relatively stable across conditions.

Within the metabolic enzyme sector, lipid-related enzymes, including those involved in precursor supply, lipid biosynthesis, and β-oxidation, account for 15–25% by mass. We observed a modest (≤ 2-fold) increase in the proteome fraction dedicated to lipid biosynthesis and precursor supply under nitrogen- and phosphorus-limited conditions, with *R. toruloides* showing a stronger increase than *Y. lipolytica* (Fig. 4 B,F). This is consistent with previous reports that nitrogen limitation does not strongly upregulate lipid biosynthetic enzymes in *Y. lipolytica* (Kerkhoven et al., 2016; Poorinmohammad et al., 2022) but does cause upregulation in *R.toruloides* (Coradetti et al., 2018b; Reķēna et al., 2023; Zhu et al., 2012). Overall protein abundance, however, decreases under nutrient limitation, and after correcting for this, we found that the absolute abundance of lipid biosynthetic enzymes (per dry cell weight) changed only modestly across all conditions (Fig. 4 C,G). The key fatty acid biosynthetic enzymes acetyl-CoA carboxylase and fatty acid synthase did increase by just over 2-fold in phosphate-limited *R. toruloides,* (Fig. S7), consistent with this being the condition with the greatest overall lipid biosynthetic flux. Thus, our results indicate that both absolute lipogenic enzyme levels and lipid synthesis fluxes are only modestly affected by nitrogen or phosphorous limitation. This supports the idea that lipid accumulation under these conditions primarily results from sustained synthesis with reduced dilution by growth.

3.4 Nitrogen limitation strongly suppresses protein synthesis

A strong change in the proteome of the nitrogen- and phosphorus-limited yeasts was the downregulation of translation machinery (Fig. 4D,H). We were curious if this aligned with decreased protein biosynthetic flux. To address this, we performed [U-$^{13}C_6$]glucose tracing using the same approach deployed for lipids to also examine protein labeling. Total cellular protein was acid hydrolyzed to free amino acids, with the labeling of valine, serine, and alanine, three abundant amino acids that are derived from glycolytic intermediates, were used as indicators of the overall proteome labeling (Fig. 5B,E; Fig. S5). All three amino acids gave similar labeling results. The fractional labeling of protein, normalized to ^{13}C-glucose tracer enrichment, was similar across batch and phosphorus-limited yeast, but 3-fold slower in nitrogen limitation (Fig. 5B,E; Fig. S9). Nitrogen limitation was also associated with the least protein abundance per dry weight (Fig. 5A,D). Together, the slowest labeling and smallest pool size implied markedly decreased protein biosynthetic flux in nitrogen limitation (about 8-fold decreased; Fig. 5C,F). Thus, in contrast to the sustained lipogenic flux, protein biosynthetic flux is dramatically suppressed in nitrogen limitation. In phosphorus limitation, the combined modest decrease in both fractional labeling rate and pool size resulted in a protein biosynthetic flux decrease of 30 - 40%. The maintenance of lipogenic flux,

when other biosynthetic processes and cell division are slowing, provides an explanation for the observed lipid accumulation.

3.5 Decreased dilution with sustained lipogenesis quantitatively aligns with the observed lipid accumulation

In growing yeasts, the lipid pool size (*X*) is maintained by constantly diluting the produced lipids (made at biosynthetic flux *v*) into expanding total cell volume due to growth at rate μ, with these two processes balanced at pseudo-steady state:

$$\frac{dX}{dt} = v - \mu X = 0 \quad (1)$$

The lipid pool size can accordingly increase by either (i) an increase of the lipid synthesis rate *v* or (ii) a reduction of the dilution due to growth μ (Fig. 6A), with steady-state lipid pool size given by

$$X = \frac{v}{\mu} \quad (2)$$

We assessed the extent to which *v* or μ predicts physiological variation in lipid pool size X, using the coefficient of determination R^2 to quantify the agreement between the predictions and experimental observations. First, we assumed that growth-related dilution is invariant (fixing the growth rate at its measured average, $\bar{\mu}$) and allowed v to vary based on experimental measurements of lipid biosynthetic flux. The resulting prediction of X using $v/\bar{\mu}$ explained a minority of the variation in the lipid abundance data ($R^2 = 0.17$; Fig. 6B). In contrast, when we assumed that v is invariant at its measured average $\bar{v}$, allowed growth rate to vary, and predicted X using $\bar{v}/\mu$, a majority of the variation in lipid abundance was explained ($R^2 = 0.51$; Fig 6C). Thus, sustained synthetic flux with decreased dilution by growth quantitatively predicts lipid pool changes in response to nutrient limitation.

Similar analysis of the factors controlling protein pool size revealed, consistent with prior literature in other microbes (Chure and Cremer, 2023; Scott et al., 2014; SCOTT and HWA, 2011), strong correlations between protein pool size, protein biosynthetic rate, and growth rate (Fig. S10). Because of these correlations, faster dilution by growth was actually associated with greater, not lesser, protein pool size, with $\bar{v}/\mu$ having negative predictive value for protein pools (Fig. S10A) despite its strong positive predictive power for lipid pools (Fig. 6C). In short, protein synthesis is downregulated in nitrogen and phosphorus limitation, whereas lipid synthesis is sustained.

Accordingly, the predominant factor controlling lipid accumulation (but not protein levels) is the rate of dilution by growth.

3.6 Chemostat data support slower dilution as the main driver of lipid accumulation

While isotope tracing is the gold standard for flux determination, fluxes can be estimated, under the assumption of minimal end-product catabolism, based on growth rate and product accumulation. Such estimates generally agreed well with measured lipid fluxes (Fig. S11). Estimated fluxes were about 2-fold lower than measured ones in nitrogen-limited yeast (with a greater discrepancy in *Y. lipolytica* than *R. toruloides*), consistent with fatty acid futile cycling in this condition (Fig. S11).

Chemostats enable steady-state nutrient-limited growth. Oleaginous yeasts grown in chemostats under nitrogen or phosphorus limitation accumulate lipids. We re-analyzed existing chemostat data for *R. toruloides* (Shen et al., 2013; Wang et al., 2018) and *Y. lipolytica* (Poorinmohammad et al., 2022) under varying degrees of nitrogen limitation, as well a single case of *R. toruloides* phosphorus limitation, estimating lipid biosynthetic flux as the lipid pool size multiplied by growth rate (which is equal to the experimenter-set chemostat dilution rate) (Fig. 7). This calculation revealed a trend towards modestly slower lipid biosynthetic flux with more severe nitrogen limitation, despite greatest lipid accumulation in this context. The single instance of phosphorus limitation showed strong lipid accumulation (~6x increase) despite only modestly higher lipid biosynthetic flux (~0.7x increase). In contrast, across both yeasts, carbon-limited chemostats do not induce lipid accumulation, despite slower growth rates (Kerkhoven et al., 2016; Shen et al., 2013), consistent with carbon limitation slowing lipogenesis and growth in parallel (Fig. S12). Thus, chemostat data reinforce the importance of both sustained lipid synthesis and reduced dilution by growth in driving lipid accumulation.

4. Discussion

Oleaginous yeasts accumulate lipids when limited for nitrogen or phosphorous. Prior work has investigated mechanisms by which such limitation promotes lipogenesis (Coradetti et al., 2018b; Kerkhoven et al., 2016; Mishra et al., 2024; Morin et al., 2011; Reķēna et al., 2023; Wang et al., 2018; Zhu et al., 2012). Lipid accumulation and lipogenesis enhancement are, however, not equivalent. Pool size can increase either due to increased synthetic flux or decreased consumption or dilution flux. We find that the primary driver of lipid accumulation in response to nitrogen or phosphorus limitation is decreased dilution by growth.

Slower growth-related dilution leads to accumulation of products whose (i) rate of synthesis is invariant and (ii) dilution exceeds overt consumption. Triglyceride stores in oleaginous yeasts during nitrogen and phosphorus limitation meet these criteria. In contrast, proteins behave in an

opposite manner as their synthesis rate is strongly suppressed in response to the nutrient stresses, leading to net depletion rather than accumulation as growth slows. Similarly, other means of slowing cell growth, such as changing the carbon source or treatment with antifungals, slow triglyceride synthesis rather than lead to triglyceride accumulation due to slower dilution (Jagtap et al., 2021; Madzak, 2021; Reķēna et al., 2023). Notably, engineered pathways may tend to be more robust than native ones in terms of maintaining flux in the face of different stressors, due to the exogenously introduced pathway enzymes being driven by strong constitutive promoters. Consistent with this, translation inhibition with cycloheximide led to lipid accumulation in an engineered *Y. lipolytica* overexpressing acetyl-CoA carboxylase and diacylglycerol transferase (Tai and Stephanopoulos, 2013; Vasdekis et al., 2017), likely reflecting sustained synthesis with slower dilution by growth. Non-native engineered "dead end" products tend to dissipate primarily by dilution rather than consumption and are particularly strong candidates for accumulation when growth slows.

For nitrogen and phosphorus limitation, which are commonly encountered environmental stressors, it is likely that mechanisms identified as enhancing lipogenesis in prior work (Pomraning et al., 2016; Ratledge and Wynn, 2002; Wang et al., 2018; Zhang et al., 2016; Zhu et al., 2012), instead act to sustain lipogenesis when many other processes slow in response to nutrient stress. For example, active pro-lipogenic regulation of transcription and translation may be required to maintain absolute lipogenic enzyme levels while the total proteome shrinks. Maintenance of lipid biosynthesis may also be favored by suppression of other competing metabolic pathways, such as amino acid biosynthesis (Kerkhoven et al., 2016; Reķēna et al., 2023; Zhu et al., 2012).

From an engineering perspective, our findings imply that nitrogen and phosphorus limitation does not markedly increase the productivity of oleaginous yeast in making triglycerides. Yields and titers can, however, be increased by directing a greater fraction of incoming resources into lipids. Titers are of particular practical importance, as they determine the cost of downstream processing to separate biodiesel from cellular components and fermentation products (Konzock and Nielsen, 2024; Tian et al., 2025). For biodiesel production, bolstering the native regulatory architecture that sustains (but does not markedly accelerate) lipid synthesis flux during nitrogen and phosphorus limitation with engineered expression of key enzymes is an appealing possibility. Phosphorus-limited *R. toruloides* display both the strongest expression of key fatty biosynthetic genes and the greatest lipogenic flux, supporting the potential for enzyme overexpression to bolster lipogenic flux in these organisms. Thus, the combination of both genetic engineering to drive flux and environmental manipulation to slow fat dilution holds the possibility to further increase biodiesel titers while also enhancing productivity.

Acknowledgments

We thank members of the Rabinowitz lab for discussions about experiments and the manuscript, S. Jagtap for the discussion about yeast physiology, M. Gupta for advice on protein regulation and proteomics data analysis, Z. Zhang for discussion about lipid synthesis flux measurement. This work was funded by Department of Energy (DOE) DE-SC0018260 to J.D.R. and M,W.; the DOE Center for Advanced Bioenergy and Bioproducts Innovation (U.S. Department of Energy, Office of Science, Biological and Environmental Research Program under Award Number DE-SC0018420) to J.D.R., C.V.R., X.L., D.R.W., Y.S. and S.R.L.; Ludwig Cancer Research funding to J.D.R. and D.R.W; NIH 35GM128813 MIRA and Princeton Catalysis Initiative to M.W. and F.C.K.; Any opinions, findings, conclusions or recommendations expressed in this publication are those of the author(s) and do not necessarily reflect the views of the US DOE.

References

Antoniewicz, M.R., 2021. A guide to metabolic flux analysis in metabolic engineering: Methods, tools and applications. Metabolic Engineering, Tools and Strategies of Metabolic Engineering 63, 2–12. https://doi.org/10.1016/j.ymben.2020.11.002

Argus, J.P., Wilks, M.Q., Zhou, Q.D., Hsieh, W.Y., Khialeeva, E., Hoi, X.P., Bui, V., Xu, S., Yu, A.K., Wang, E.S., Herschman, H.R., Williams, K.J., Bensinger, S.J., 2018. Development and Application of FASA, a Model for Quantifying Fatty Acid Metabolism Using Stable Isotope Labeling. Cell Reports 25, 2919-2934.e8. https://doi.org/10.1016/j.celrep.2018.11.041

Barth, G., Gaillardin, C., 1996. Yarrowia lipolytica, in: Wolf, K. (Ed.), Nonconventional Yeasts in Biotechnology: A Handbook. Springer, Berlin, Heidelberg, pp. 313–388. https://doi.org/10.1007/978-3-642-79856-6_10

Blazeck, J., Hill, A., Liu, L., Knight, R., Miller, J., Pan, A., Otoupal, P., Alper, H.S., 2014. Harnessing Yarrowia lipolytica lipogenesis to create a platform for lipid and biofuel production. Nat Commun 5, 3131. https://doi.org/10.1038/ncomms4131

Boer, V.M., Crutchfield, C.A., Bradley, P.H., Botstein, D., Rabinowitz, J.D., 2010. Growth-limiting intracellular metabolites in yeast growing under diverse nutrient limitations. Mol. Biol. Cell 21, 198–211.

Chmielarz, M., Blomqvist, J., Sampels, S., Sandgren, M., Passoth, V., 2021. Microbial lipid production from crude glycerol and hemicellulosic hydrolysate with oleaginous yeasts. Biotechnology for Biofuels 14, 65. https://doi.org/10.1186/s13068-021-01916-y

Chure, G., Cremer, J., 2023. An optimal regulation of fluxes dictates microbial growth in and out of steady state. eLife 12, e84878. https://doi.org/10.7554/eLife.84878

Coradetti, S.T., Pinel, D., Geiselman, G.M., Ito, M., Mondo, S.J., Reilly, M.C., Cheng, Y.-F., Bauer, S., Grigoriev, I.V., Gladden, J.M., Simmons, B.A., Brem, R.B., Arkin, A.P., Skerker, J.M., 2018a. Functional genomics of lipid metabolism in the oleaginous yeast Rhodosporidium toruloides. eLife 7, e32110. https://doi.org/10.7554/eLife.32110

Coradetti, S.T., Pinel, D., Geiselman, G.M., Ito, M., Mondo, S.J., Reilly, M.C., Cheng, Y.-F., Bauer, S., Grigoriev, I.V., Gladden, J.M., Simmons, B.A., Brem, R.B., Arkin, A.P., Skerker, J.M., 2018b. Functional genomics of lipid metabolism in the oleaginous yeast Rhodosporidium toruloides. eLife 7, e32110. https://doi.org/10.7554/eLife.32110

Dias, B., Fernandes, H., Lopes, M., Belo, I., 2023. Yarrowia lipolytica produces lipid-rich biomass in medium mimicking lignocellulosic biomass hydrolysate. Appl Microbiol Biotechnol 107, 3925–3937. https://doi.org/10.1007/s00253-023-12565-6

Dinh, H.V., Suthers, P.F., Chan, S.H.J., Shen, Y., Xiao, T., Deewan, A., Jagtap, S.S., Zhao, H., Rao, C.V., Rabinowitz, J.D., Maranas, C.D., 2019. A comprehensive genome-scale model for Rhodosporidium toruloides IFO0880 accounting for functional genomics and phenotypic data. Metab Eng Commun 9, e00101.

Edwards, A., Haas, W., 2016. Multiplexed Quantitative Proteomics for High-Throughput Comprehensive Proteome Comparisons of Human Cell Lines. Methods Mol Biol 1394, 1–13. https://doi.org/10.1007/978-1-4939-3341-9_1

Gopalakrishnan, S., Maranas, C.D., 2015. 13C metabolic flux analysis at a genome-scale. Metabolic Engineering 32, 12–22. https://doi.org/10.1016/j.ymben.2015.08.006

Gupta, M., Sonnett, M., Ryazanova, L., Presler, M., Wühr, M., 2018. Quantitative Proteomics of Xenopus Embryos I, Sample Preparation. Methods Mol Biol 1865, 175–194. https://doi.org/10.1007/978-1-4939-8784-9_13

Hellerstein, M.K., Neese, R.A., 1992. Mass isotopomer distribution analysis: a technique for measuring biosynthesis and turnover of polymers. American Journal of Physiology-Endocrinology and Metabolism 263, E988-1001. https://doi.org/10.1152/ajpendo.1992.263.5.E988

Hu, C., Zhao, X., Zhao, J., Wu, S., Zhao, Z.K., 2009. Effects of biomass hydrolysis by-products on oleaginous yeast Rhodosporidium toruloides. Bioresour. Technol. 100, 4843–4847.

Hughes, C.S., Moggridge, S., Müller, T., Sorensen, P.H., Morin, G.B., Krijgsveld, J., 2019. Single-pot, solid-phase-enhanced sample preparation for proteomics experiments. Nat Protoc 14, 68–85. https://doi.org/10.1038/s41596-018-0082-x

Jagtap, S.S., Deewan, A., Liu, J.-J., Walukiewicz, H.E., Yun, E.J., Jin, Y.-S., Rao, C.V., 2021. Integrating transcriptomic and metabolomic analysis of the oleaginous yeast Rhodosporidium toruloides IFO0880 during growth under different carbon sources. Appl Microbiol Biotechnol 105, 7411–7425. https://doi.org/10.1007/s00253-021-11549-8

Jang, C., Chen, L., Rabinowitz, J.D., 2018. Metabolomics and Isotope Tracing. Cell 173, 822–837.

Kelleher, J.K., Masterson, T.M., 1992. Model equations for condensation biosynthesis using stable isotopes and radioisotopes. American Journal of Physiology-Endocrinology and Metabolism 262, E118–E125. https://doi.org/10.1152/ajpendo.1992.262.1.E118

Kerkhoven, E.J., Pomraning, K.R., Baker, S.E., Nielsen, J., 2016. Regulation of amino-acid metabolism controls flux to lipid accumulation in Yarrowia lipolytica. npj Syst Biol Appl 2, 1–7. https://doi.org/10.1038/npjsba.2016.5

Konzock, O., Nielsen, J., 2024. TRYing to evaluate production costs in microbial biotechnology. Trends in Biotechnology 42, 1339–1347. https://doi.org/10.1016/j.tibtech.2024.04.007

Lee, W.D., Weilandt, D.R., Liang, L., MacArthur, M.R., Jaiswal, N., Ong, O., Mann, C.G., Chu, Q., Hunter, C.J., Ryseck, R.-P., Lu, W., Oschmann, A.M., Cowan, A.J., TeSlaa, T.A., Bartman, C.R., Jang, C., Baur, J.A., Titchenell, P.M., Rabinowitz, J.D., 2025. Lactate homeostasis is maintained through regulation of glycolysis and lipolysis. Cell Metabolism 37, 758-771.e8. https://doi.org/10.1016/j.cmet.2024.12.009

Lücking, R., Huhndorf ,Sabine, Pfister ,Donald H., Plata ,Eimy Rivas, and Lumbsch, H.T., 2009. Fungi evolved right on track. Mycologia 101, 810–822. https://doi.org/10.3852/09-016

Madzak, C., 2021. Yarrowia lipolytica Strains and Their Biotechnological Applications: How Natural Biodiversity and Metabolic Engineering Could Contribute to Cell Factories Improvement. Journal of Fungi 7, 548. https://doi.org/10.3390/jof7070548

Martín, H.G., Kumar, V.S., Weaver, D., Ghosh, A., Chubukov, V., Mukhopadhyay, A., Arkin, A., Keasling, J.D., 2015. A Method to Constrain Genome-Scale Models with 13C Labeling Data. PLOS Computational Biology 11, e1004363. https://doi.org/10.1371/journal.pcbi.1004363

McAlister, G.C., Nusinow, D.P., Jedrychowski, M.P., Wühr, M., Huttlin, E.L., Erickson, B.K., Rad, R., Haas, W., Gygi, S.P., 2014. MultiNotch MS3 Enables Accurate, Sensitive, and Multiplexed Detection of Differential Expression across Cancer Cell Line Proteomes. Anal. Chem. 86, 7150–7158. https://doi.org/10.1021/ac502040v

Metzl-Raz, E., Kafri, M., Yaakov, G., Soifer, I., Gurvich, Y., Barkai, N., 2017. Principles of cellular resource allocation revealed by condition-dependent proteome profiling. Elife 6.

Mishra, S., Deewan, A., Zhao, H., Rao, C.V., 2024. Nitrogen starvation causes lipid remodeling in Rhodotorula toruloides. Microbial Cell Factories 23. https://doi.org/10.1186/s12934-024-02414-0

Morin, N., Cescut, J., Beopoulos, A., Lelandais, G., Berre, V.L., Uribelarrea, J.-L., Molina-Jouve, C., Nicaud, J.-M., 2011. Transcriptomic Analyses during the Transition from Biomass Production to Lipid Accumulation in the Oleaginous Yeast Yarrowia lipolytica. PLOS ONE 6, e27966. https://doi.org/10.1371/journal.pone.0027966

Nelson, D.L., Cox, M., n.d. Lehninger principles of biochemistry, 7th ed. W.H. Freeman, New York, NY.

Park, Y.-K., Ledesma-Amaro, R., 2023. What makes Yarrowia lipolytica well suited for industry? Trends in Biotechnology 41, 242–254. https://doi.org/10.1016/j.tibtech.2022.07.006

Perez-Riverol, Y., Csordas, A., Bai, J., Bernal-Llinares, M., Hewapathirana, S., Kundu, D.J., Inuganti, A., Griss, J., Mayer, G., Eisenacher, M., Pérez, E., Uszkoreit, J., Pfeuffer, J., Sachsenberg, T., Yılmaz, Ş., Tiwary, S., Cox, J., Audain, E., Walzer, M., Jarnuczak, A.F., Ternent, T., Brazma, A., Vizcaíno, J.A., 2019. The PRIDE database and related tools and resources in 2019: improving support for

quantification data. Nucleic Acids Research 47, D442–D450. https://doi.org/10.1093/nar/gky1106

Pomraning, K.R., Kim, Y.-M., Nicora, C.D., Chu, R.K., Bredeweg, E.L., Purvine, S.O., Hu, D., Metz, T.O., Baker, S.E., 2016. Multi-omics analysis reveals regulators of the response to nitrogen limitation in Yarrowia lipolytica. BMC Genomics 17, 138.

Poorinmohammad, N., Fu, J., Wabeke, B., Kerkhoven, E.J., 2022. Validated Growth Rate-Dependent Regulation of Lipid Metabolism in Yarrowia lipolytica. International Journal of Molecular Sciences 23, 8517. https://doi.org/10.3390/ijms23158517

Qiao, K., Wasylenko, T.M., Zhou, K., Xu, P., Stephanopoulos, G., 2017. Lipid production in Yarrowia lipolytica is maximized by engineering cytosolic redox metabolism. Nat. Biotechnol. 35, 173–177.

Qin, J., Kurt, E., LBassi, T., Sa, L., Xie, D., 2023. Biotechnological production of omega-3 fatty acids: current status and future perspectives. Front Microbiol 14, 1280296. https://doi.org/10.3389/fmicb.2023.1280296

Rappsilber, J., Mann, M., Ishihama, Y., 2007. Protocol for micro-purification, enrichment, pre-fractionation and storage of peptides for proteomics using StageTips. Nat Protoc 2, 1896–1906. https://doi.org/10.1038/nprot.2007.261

Ratledge, C., 2010. 1 - Single Cell Oils for the 21st Century, in: Cohen, Z., Ratledge, C. (Eds.), Single Cell Oils (Second Edition). AOCS Press, pp. 3–26. https://doi.org/10.1016/B978-1-893997-73-8.50005-0

Ratledge, C., Wynn, J.P., 2002. The biochemistry and molecular biology of lipid accumulation in oleaginous microorganisms. Adv Appl Microbiol 51, 1–51. https://doi.org/10.1016/s0065-2164(02)51000-5

Reķēna, A., Pinheiro, M.J., Bonturi, N., Belouah, I., Tammekivi, E., Herodes, K., Kerkhoven, E.J., Lahtvee, P.-J., 2023. Genome-scale metabolic modeling reveals metabolic trade-offs associated with lipid production in Rhodotorula toruloides. PLoS Comput. Biol. 19, e1011009.

Saini, R., Hegde, K., Osorio-Gonzalez, C.S., Brar, S.K., Vezina, P., 2020. Evaluating the Potential of Rhodosporidium toruloides-1588 for High Lipid Production Using Undetoxified Wood Hydrolysate as a Carbon Source. Energies 13, 5960. https://doi.org/10.3390/en13225960

Sauer, U., 2006. Metabolic networks in motion: 13C-based flux analysis. Mol. Syst. Biol. 2, 62.

Schaechter, M., Maaloe, O., Kjeldgaard, N.O., 1958. Dependency on medium and temperature of cell size and chemical composition during balanced grown of Salmonella typhimurium. J Gen Microbiol 19, 592–606. https://doi.org/10.1099/00221287-19-3-592

Schweppe, D.K., Eng, J.K., Yu, Q., Bailey, D., Rad, R., Navarrete-Perea, J., Huttlin, E.L., Erickson, B.K., Paulo, J.A., Gygi, S.P., 2020. Full-Featured, Real-Time Database Searching Platform Enables Fast and Accurate Multiplexed Quantitative Proteomics. J Proteome Res 19, 2026–2034. https://doi.org/10.1021/acs.jproteome.9b00860

SCOTT, M., HWA, T., 2011. Bacterial growth laws and their applications. Curr Opin Biotechnol 22, 559–565. https://doi.org/10.1016/j.copbio.2011.04.014

Scott, M., Klumpp, S., Mateescu, E.M., Hwa, T., 2014. Emergence of robust growth laws from optimal regulation of ribosome synthesis. Mol. Syst. Biol. 10, 747.

Shen, H., Gong, Z., Yang, X., Jin, G., Bai, F., Zhao, Z.K., 2013. Kinetics of continuous cultivation of the oleaginous yeast Rhodosporidium toruloides. J. Biotechnol. 168, 85–89.

Shen, Q., Chen, Y., Jin, D., Lin, H., Wang, Q., Zhao, Y.-H., 2016. Comparative genome analysis of the oleaginous yeast *Trichosporon fermentans* reveals its potential applications in lipid accumulation. Microbiological Research 192, 203–210. https://doi.org/10.1016/j.micres.2016.07.005

Shen, Y., Dinh, H.V., Cruz, E.R., Chen, Z., Bartman, C.R., Xiao, T., Call, C.M., Ryseck, R.-P., Pratas, J., Weilandt, D., Baron, H., Subramanian, A., Fatma, Z., Wu, Z.-Y., Dwaraknath, S., Hendry, J.I., Tran, V.G., Yang, L., Yoshikuni, Y., Zhao, H., Maranas, C.D., Wühr, M., Rabinowitz, J.D., 2024. Mitochondrial ATP generation is more proteome efficient than glycolysis. Nat Chem Biol 1–10. https://doi.org/10.1038/s41589-024-01571-y

Sonnett, M., Gupta, M., Nguyen, T., Wühr, M., 2018. Quantitative Proteomics for Xenopus Embryos II, Data Analysis. Methods Mol Biol 1865, 195–215. https://doi.org/10.1007/978-1-4939-8784-9_14

Su, X., Lu, W., Rabinowitz, J.D., 2017. Metabolite Spectral Accuracy on Orbitraps. Anal Chem 89, 5940–5948. https://doi.org/10.1021/acs.analchem.7b00396

Tai, M., Stephanopoulos, G., 2013. Engineering the push and pull of lipid biosynthesis in oleaginous yeast Yarrowia lipolytica for biofuel production. Metab Eng 15, 1–9. https://doi.org/10.1016/j.ymben.2012.08.007

Taylor, J.W., and Berbee, M.L., 2006. Dating divergences in the Fungal Tree of Life: review and new analyses. Mycologia 98, 838–849. https://doi.org/10.1080/15572536.2006.11832614

Tian, Y., Yang, L., Ding, S., Zhang, D., Yuan, L., Liu, Z., Hu, Q.-N., 2025. BioTRY: A Comprehensive Knowledge Base for Titer, Rate, and Yield of Biosynthesis. ACS Synth. Biol. 14, 285–289. https://doi.org/10.1021/acssynbio.4c00347

Tiukova, I.A., Brandenburg, J., Blomqvist, J., Sampels, S., Mikkelsen, N., Skaugen, M., Arntzen, M.Ø., Nielsen, J., Sandgren, M., Kerkhoven, E.J., 2019. Proteome analysis of xylose metabolism in Rhodotorula toruloides during lipid production. Biotechnol. Biofuels 12, 137.

Tumanov, S., Bulusu, V., Kamphorst, J.J., 2015. Analysis of Fatty Acid Metabolism Using Stable Isotope Tracers and Mass Spectrometry, in: Methods in Enzymology. Elsevier, pp. 197–217. https://doi.org/10.1016/bs.mie.2015.05.017

Vasdekis, A.E., Silverman, A.M., Stephanopoulos, G., 2017. Exploiting Bioprocessing Fluctuations to Elicit the Mechanistics of De Novo Lipogenesis in Yarrowia lipolytica. PLoS One 12, e0168889.

Wakil, S.J., 1989. Fatty acid synthase, a proficient multifunctional enzyme. Biochemistry 28, 4523–4530. https://doi.org/10.1021/bi00437a001

Wang, Y., Zhang, S., Zhu, Z., Shen, H., Lin, X., Jin, X., Jiao, X., Zhao, Z.K., 2018. Systems analysis of phosphate-limitation-induced lipid accumulation by the oleaginous yeast Rhodosporidium toruloides. Biotechnol Biofuels 11, 148. https://doi.org/10.1186/s13068-018-1134-8

Wasylenko, T.M., Ahn, W.S., Stephanopoulos, G., 2015. The oxidative pentose phosphate pathway is the primary source of NADPH for lipid overproduction from glucose in Yarrowia lipolytica. Metab. Eng. 30, 27–39.

Xia, J., Sánchez, B.J., Chen, Y., Campbell, K., Kasvandik, S., Nielsen, J., 2022. Proteome allocations change linearly with the specific growth rate of Saccharomyces cerevisiae under glucose limitation. Nat. Commun. 13, 2819.

Xie, D., Jackson, E.N., Zhu, Q., 2015. Sustainable source of omega-3 eicosapentaenoic acid from metabolically engineered Yarrowia lipolytica: from fundamental research to commercial production. Appl Microbiol Biotechnol 99, 1599–1610. https://doi.org/10.1007/s00253-014-6318-y

Yang, E., Xu, L., Yang, Y., Zhang, X., Xiang, M., Wang, C., An, Z., Liu, X., 2012. Origin and evolution of carnivorism in the Ascomycota (fungi). Proceedings of the National Academy of Sciences 109, 10960–10965. https://doi.org/10.1073/pnas.1120915109

Yuan, J., Bennett, B.D., Rabinowitz, J.D., 2008. Kinetic flux profiling for quantitation of cellular metabolic fluxes. Nat. Protoc. 3, 1328–1340.

Yuan, J., Fowler, W.U., Kimball, E., Lu, W., Rabinowitz, J.D., 2006. Kinetic flux profiling of nitrogen assimilation in Escherichia coli. Nat Chem Biol 2, 529–530. https://doi.org/10.1038/nchembio816

Zhang, H., Wu, C., Wu, Q., Dai, J., Song, Y., 2016. Metabolic Flux Analysis of Lipid Biosynthesis in the Yeast Yarrowia lipolytica Using 13C-Labled Glucose and Gas Chromatography-Mass Spectrometry. PLoS One 11, e0159187.

Zhang, Z., Chen, L., Liu, L., Su, X., Rabinowitz, J.D., 2017. Chemical Basis for Deuterium Labeling of Fat and NADPH. J. Am. Chem. Soc. 139, 14368–14371.

Zhang, Z., TeSlaa, T., Xu, X., Zeng, X., Yang, L., Xing, G., Tesz, G.J., Clasquin, M.F., Rabinowitz, J.D., 2021. Serine catabolism generates liver NADPH and supports hepatic lipogenesis. Nat Metab 3, 1608–1620.

Zhu, Z., Zhang, S., Liu, H., Shen, H., Lin, X., Yang, F., Zhou, Y.J., Jin, G., Ye, M., Zou, H., Zhao, Z.K., 2012. A multi-omic map of the lipid-producing yeast Rhodosporidium toruloides. Nat Commun 3, 1112. https://doi.org/10.1038/ncomms2112

Figures and Tables

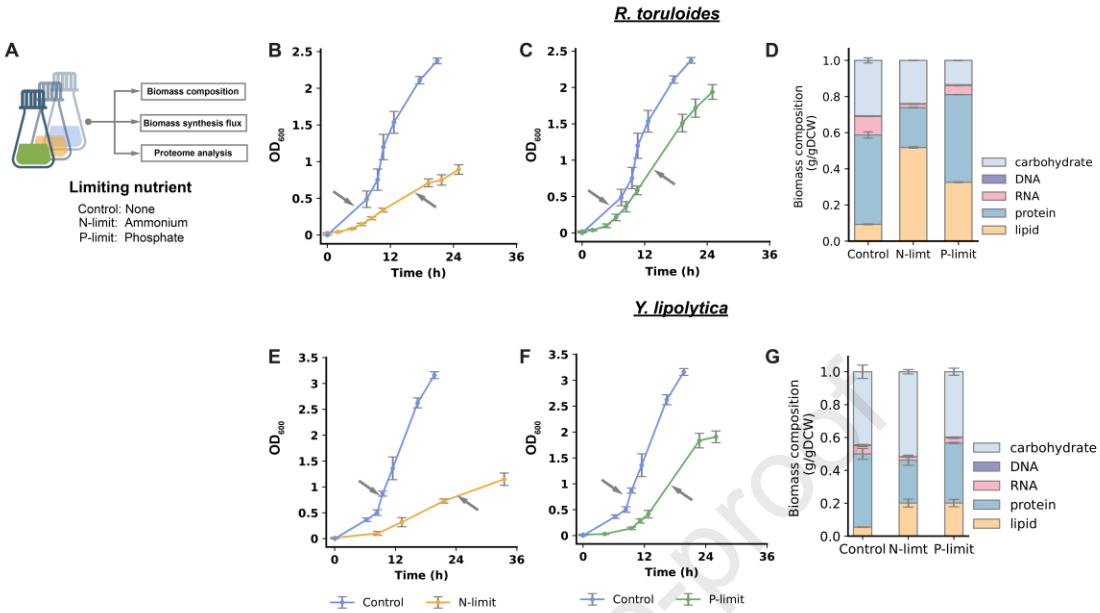

Fig. 1. Limitation for nitrogen (ammonia) or phosphorous (phosphate) in oleaginous yeast triggers lipid accumulation. (A) Schematic of the experimental design. (B,C) Growth curves for *R. toruloides.* Arrows indicate when samples were taken. (D) Biomass composition across different nutrient conditions. (E-G) Same for *Y. lipolytica.* Control = nutrient replete. Mean ± *s.d.*, *n* = 3 biological replicates.

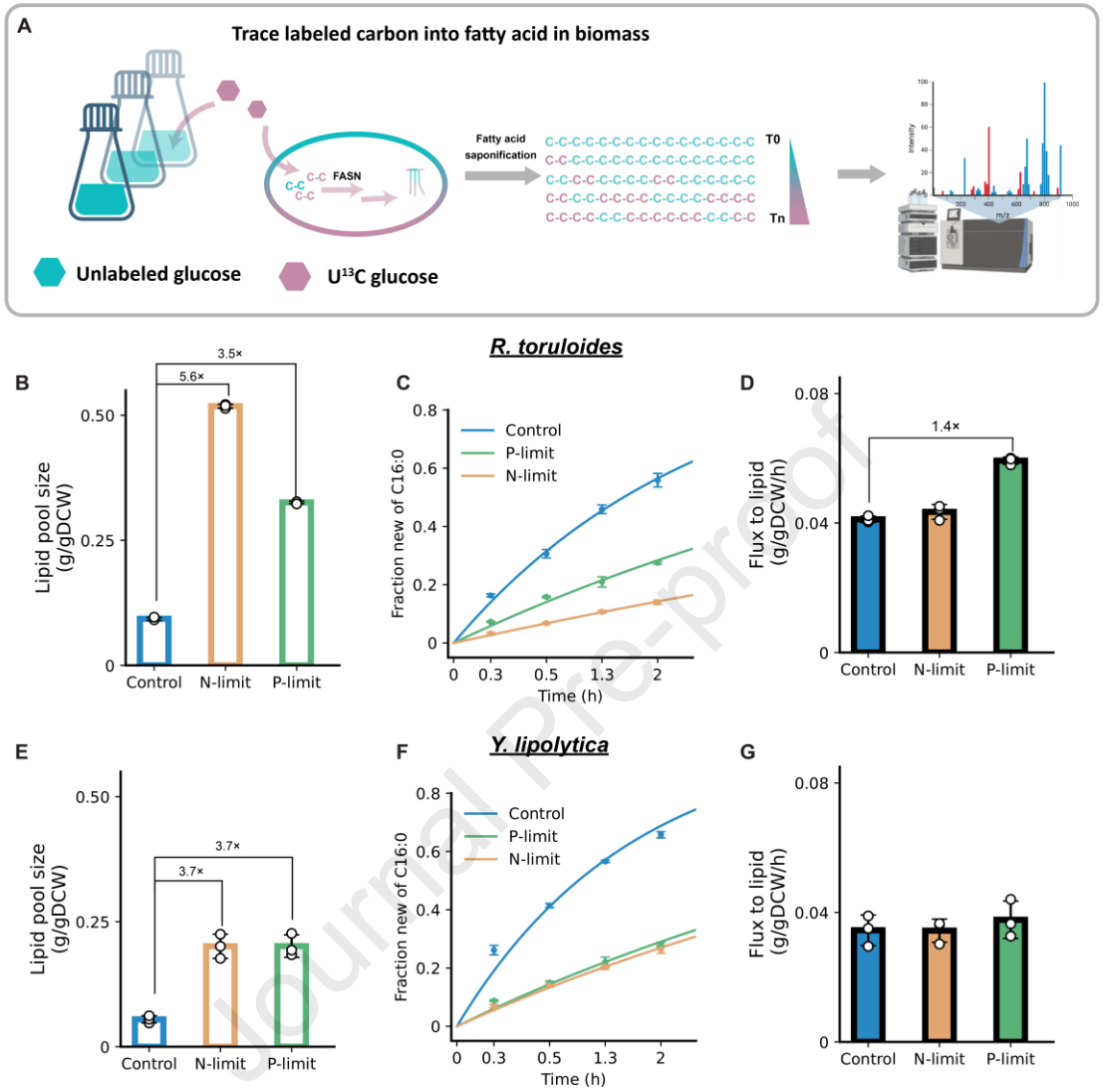

Fig. 2. Nutrient limitation leads to lipid accumulation without comparable increases in lipid flux. (A) Schematic of the experimental design, which involves introducing ^{13}C-labeled glucose and monitoring the kinetics of accumulation of labeled fatty acid tails in lipids. (B) Lipid pool sizes (per gram dry cell weight) in freely growing or nutrient-limited *R. toruloides.* (C) Fatty acid labeling kinetics. (D) Synthetic flux to lipid biomass, which is the product of pool size from (B) and the exponential rate constant from (C). (E – G). Same for *Y. lipolytica*. Mean ± *s.d*., *n* = 3 biological replicates.

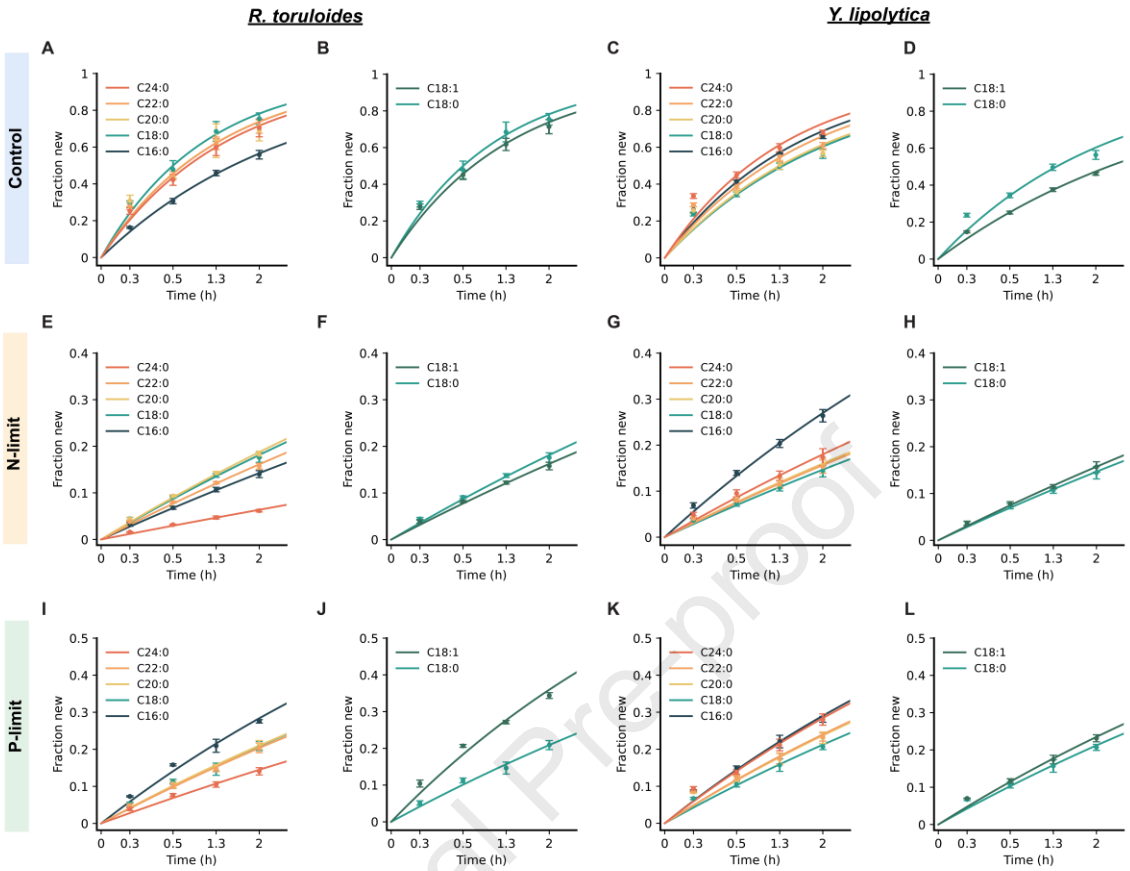

863 **Fig. 3.** Different fatty acids show similar labeling kinetics. (A-D) Nutrient-replete (control) condition
864 for the indicated organism and fatty acids. (E-H) Nitrogen limitation. (I-L) Phosphorus limitation. For
865 quantitative total flux to lipid based on the combined data from palmitate, oleate, and linoleate, see
866 Figure S5. Mean ± *s.d*, *n* = 3 biological replicates.
867

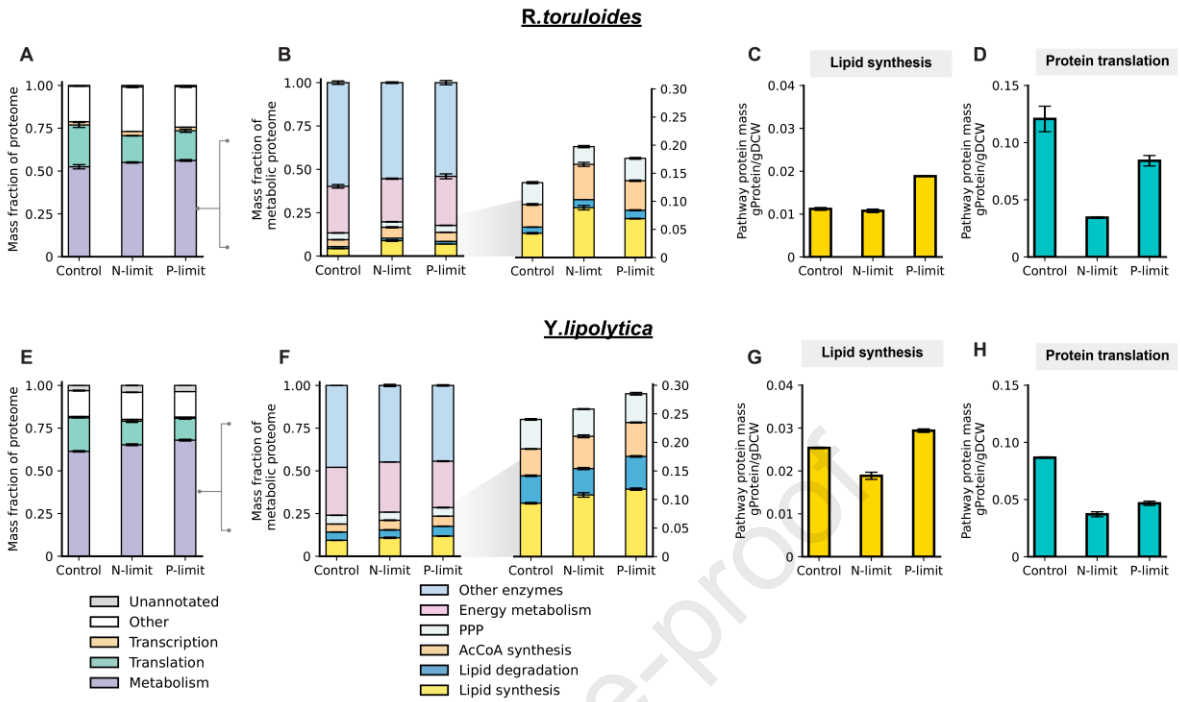

Fig. 4. Proteome analysis reveals that nutrient limitation only modestly changes overall lipid biosynthetic enzyme levels. (A) Fractional abundance of major proteome sectors in freely growing and nutrient-limited *R. toruloides.* (B) Fractional abundance of the metabolic proteome relative to whole cell protein (zoomed-in view of the lipid-related enzymes to the right). (C) Absolute abundance in biomass of lipid biosynthesis enzymes. (D) Absolute abundance in biomass of translation machinery. (E – H) Same for *Y. lipolytica.* Mean ± *s.d*, *n* = 3 biological replicates.

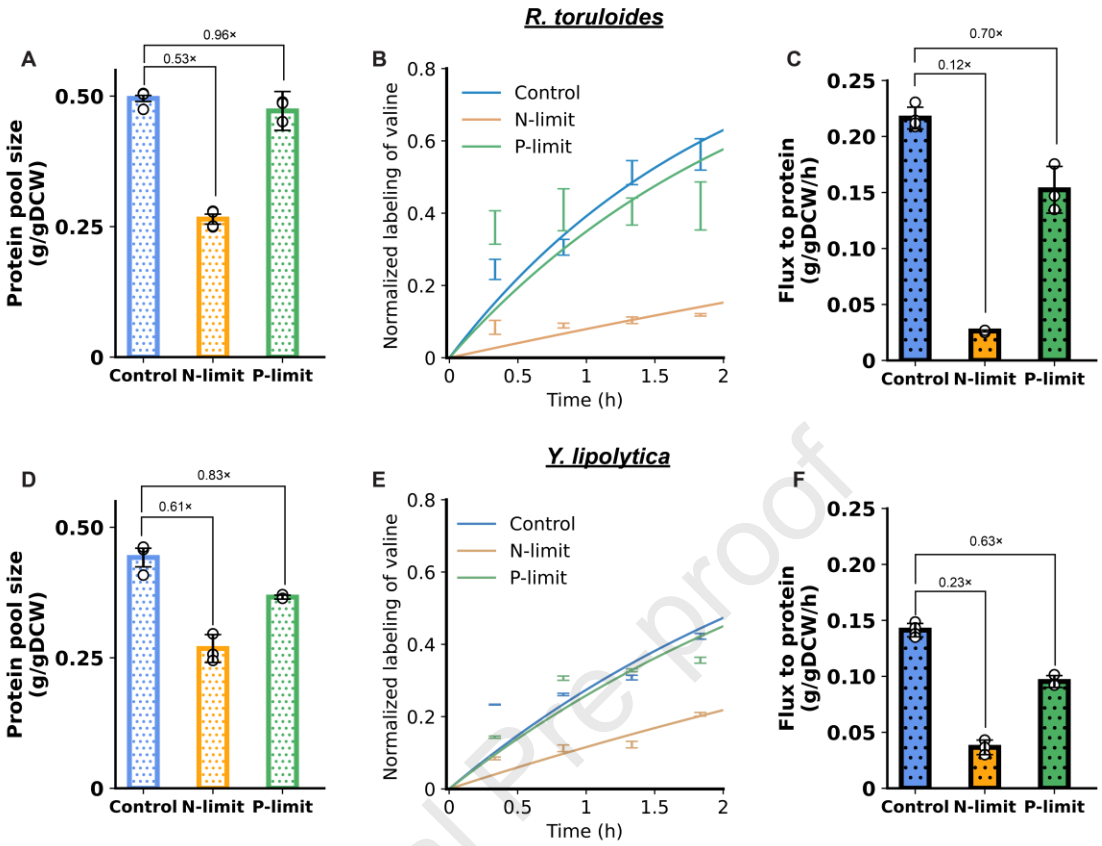

875 **Fig. 5**. Protein synthesis is strongly suppressed under nitrogen limitation. (A) Protein pool sizes
876 (per gram dry cell weight) in freely growing or nutrient-limited *R. toruloides*. (B) Protein labeling
877 kinetics (based on labeling of valine from hydrolyzed whole cell protein). (C) Protein synthetic flux,
878 which is the product of pool size from (A) and the exponential rate constant from (B). (D – F). Same
879 for *Y. lipolytica*. Mean ± *s.d.*, *n* = 3 biological replicates.

880

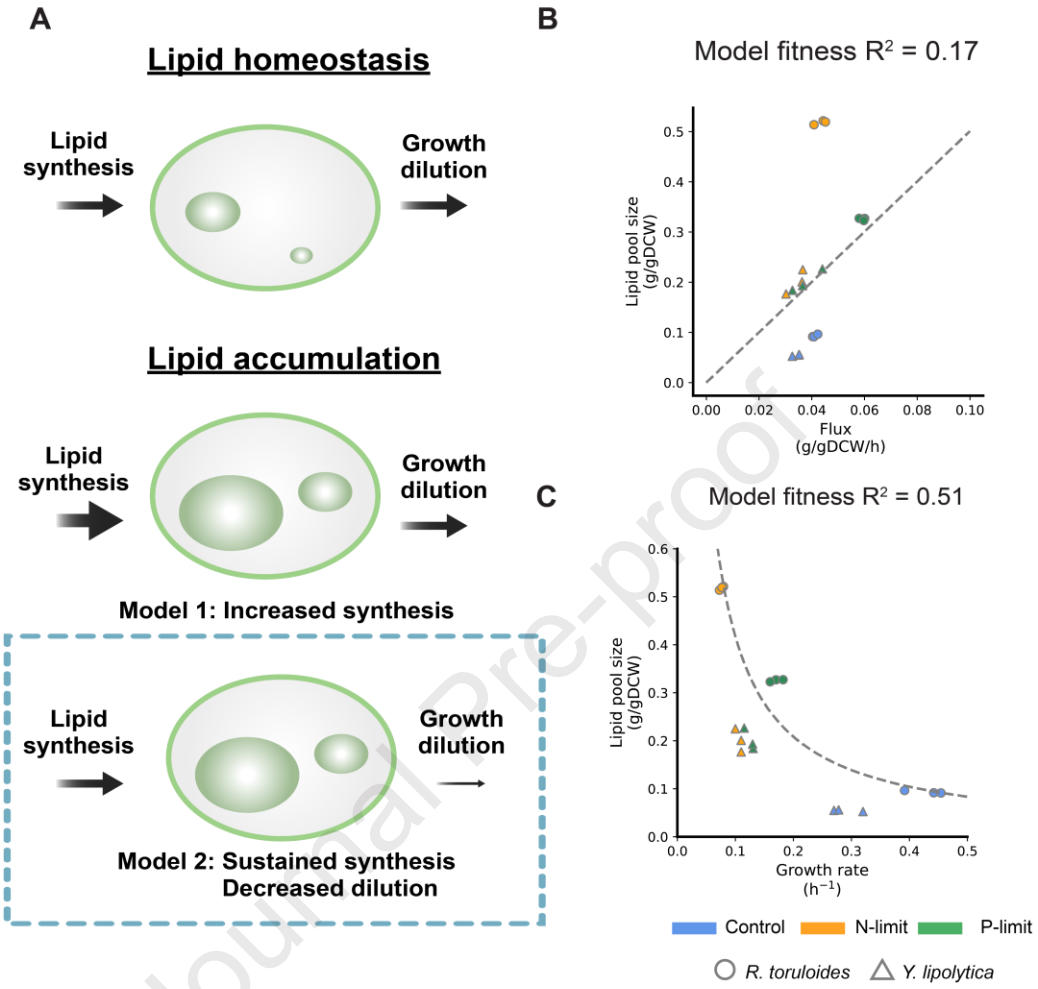

881 **Fig.6**. Lipid accumulation in response to nutrient limitation can be quantitatively explained by the
882 combination of sustained synthesis and decreased growth-related dilution. (A) Two models for lipid
883 accumulation in response to nutrient limitation. In the top model, lipid synthesis increases. In the
884 bottom model, lipid synthesis is sustained, combined with slower growth-related dilution. (B)
885 Predicted and observed lipid pool sizes based on experimentally observed biosynthetic flux and
886 fixed growth rate. The fit is poor, reflecting the importance of varying growth rate in controlling lipid
887 pools. (C) The same analysis, but holding biosynthetic flux constant and varying growth rate. The
888 fit is good, reflecting lipid accumulation in response to nutrient limitation, largely occurring due to
889 slowing of growth. In (B) and (C), individual experimental data points are shown as circles for *R.*
890 *toruloides* and triangulars for *Y. lipolytica* with colors indicating the nutrient conditions.

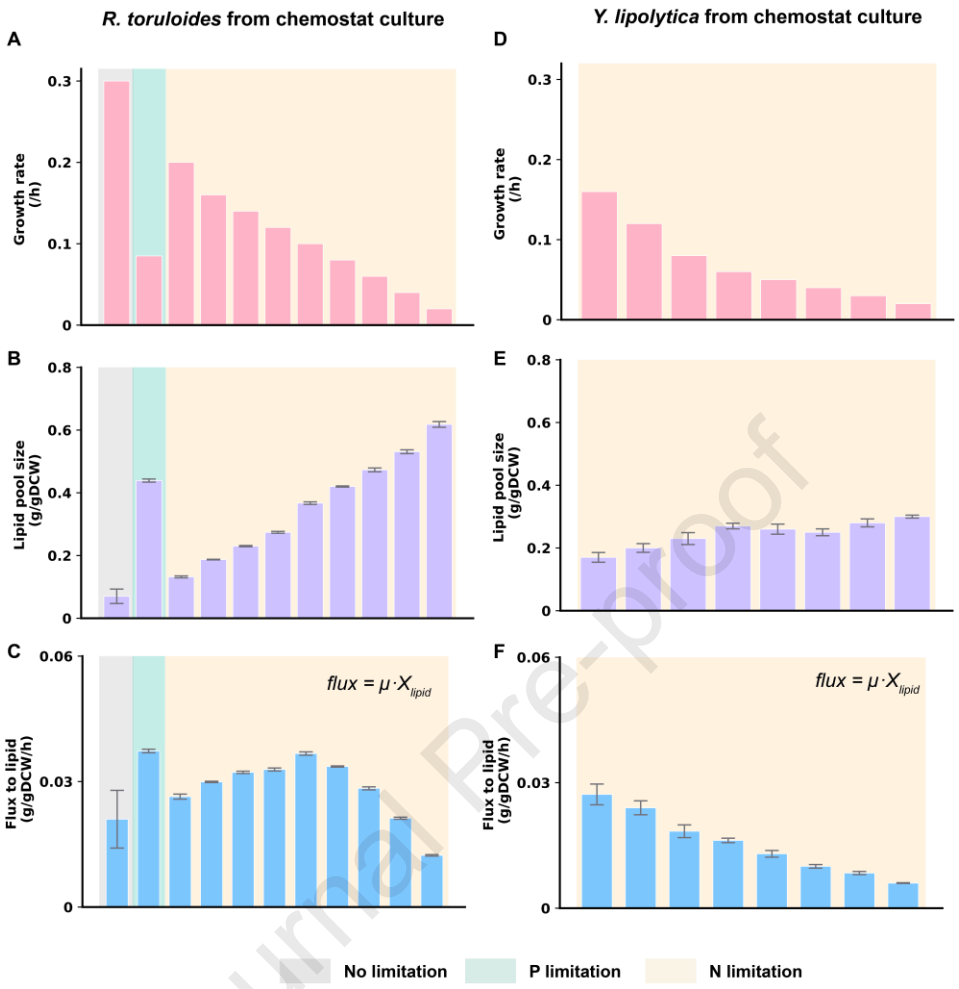

Fig. 7. Nutrient limitation in chemostats leads to lipid accumulation without comparable increases in lipid flux. (A) Steady-state growth rate of *R. toruloides* AS 2.1389 strain under no limitation, chemostat culture with phosphorus limitation (single growth rate), or chemostat culture with nitrogen limitation of increasing stringency from left to right, using published data from Wang *et al*. (4) and Shen *et al*. (Shen et al., 2013) (B) Associated lipid pool sizes. (C) Calculated lipid biosynthetic, which is the product of growth rate from (A) and pool size from (B). (D-F). Same for *Y. lipolytica* OKL049 strain, with the available data limited to nitrogen limited chemostat of increasing stringency, using published data from Poorinmohammad *et al*. (Poorinmohammad et al., 2022)

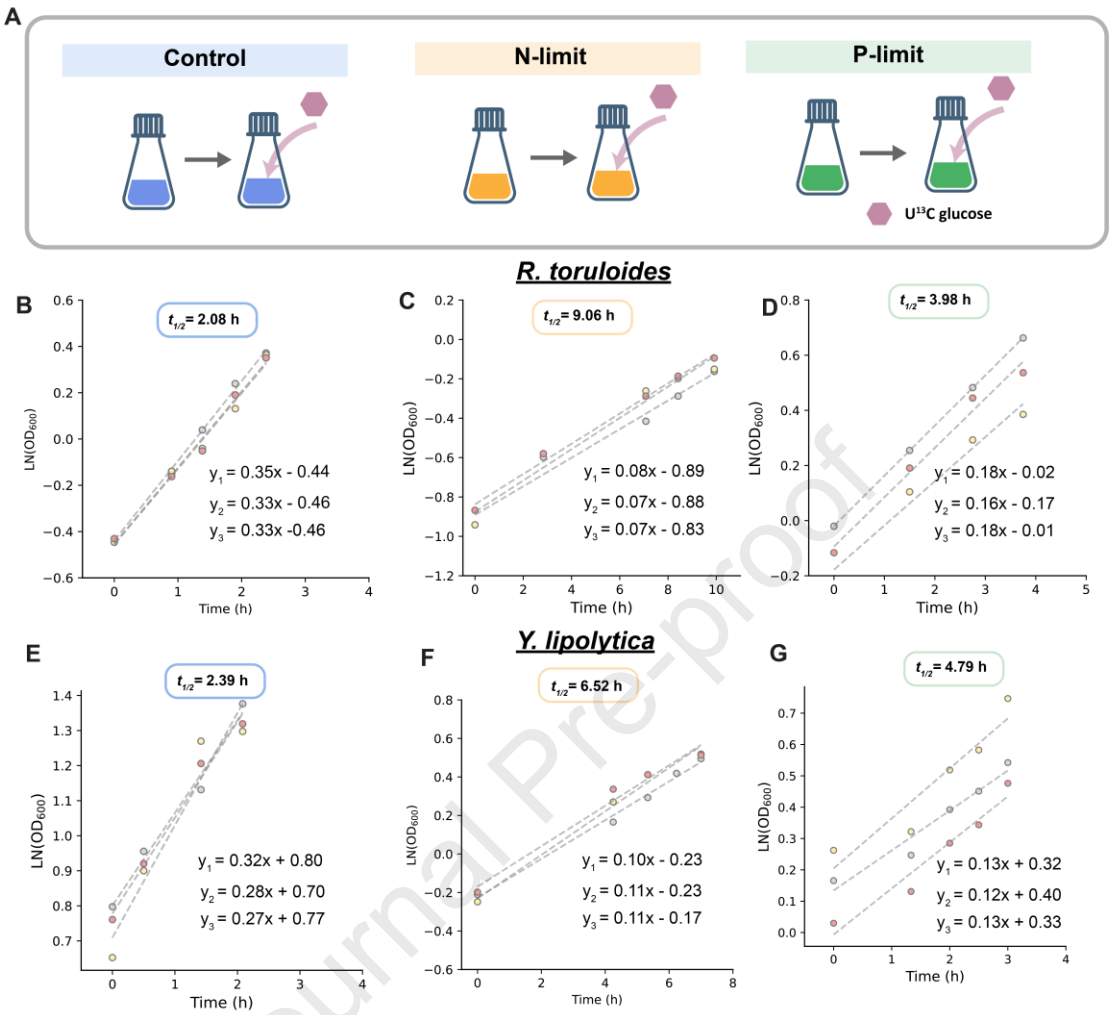

Fig. S1. Nutrient limitation is maintained during the tracing experiments. (A) Schematic of the media composition during the tracing experiment. (B – D) Logarithmic OD_{600} measured during the indicated tracing experiments for *R. toruloides*. (E-G) same for *Y. lipolytica.* Growth rates were calculated from each experiment by linear fitting. Doubling times ($t_{1/2}$) were estimated using the average growth rate.

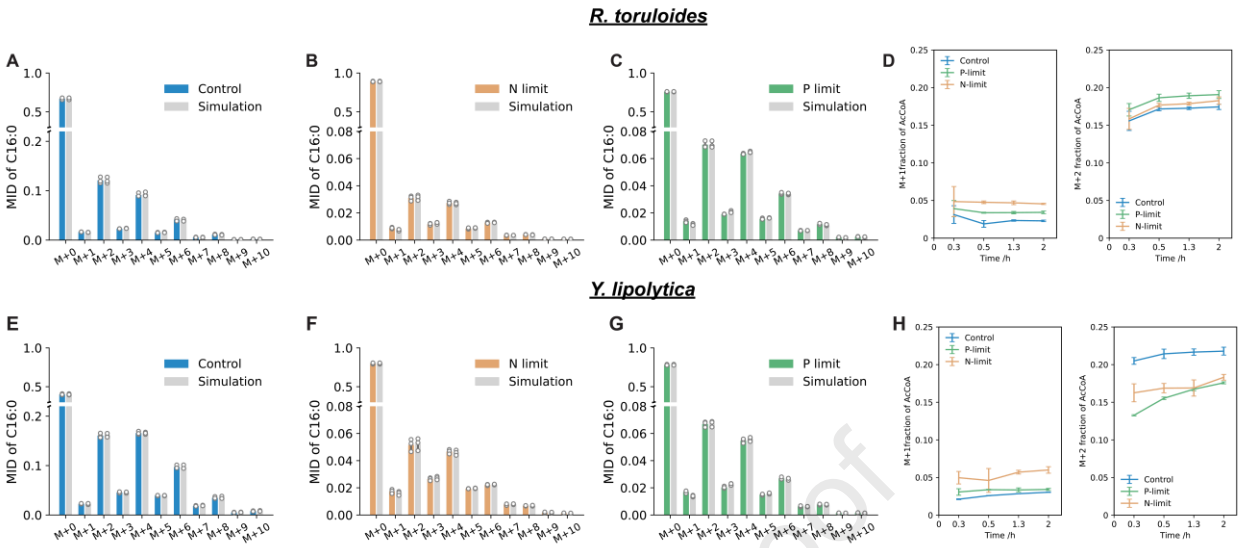

907

908 Fig. S2. Fatty acid labeling patterns reflect condensation of two-carbon units. Experimental mass
909 isotopologue distribution (MID) and simulated labeling pattern of palmitate (C16:0) (data shown is
910 from 110 min time point from *R. toruloides* culture in 25% [U-$^{13}C_6$]glucose) under (A) control
911 condition; (B) under nitrogen limitation, and (C) under phosphorus limitation. (D) Inferred acetyl-
912 CoA labeling as a function of time based on fitting MIDs as shown in (A-C) based on trinomial
913 condensation of [M + 0, M + 1, M + 2] acetyl-CoA. (E-G) Same for *Y. lipolytica.* Mean ± *s.d.*, *n* = 3
914 biological replicates.

915

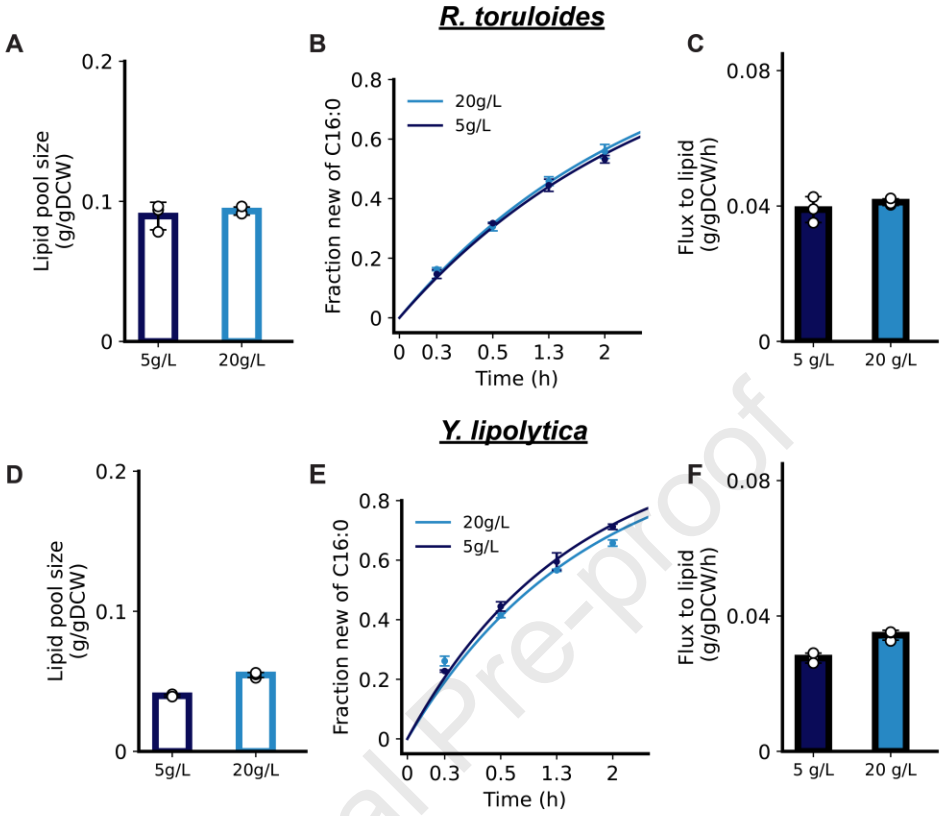

Fig. S3. Comparable lipid synthesis between 5 g/L and 20 g/L glucose in control cultures. (A) Lipid pool sizes in R. *toruloides* grown freely with 5 g/L or 20 g/L glucose. (B) Fatty acid labeling kinetics. (C) Synthetic flux to lipid biomass. (D–F) Same for Y. lipolytica. Mean ± s.d., n = 3 biological replicates.

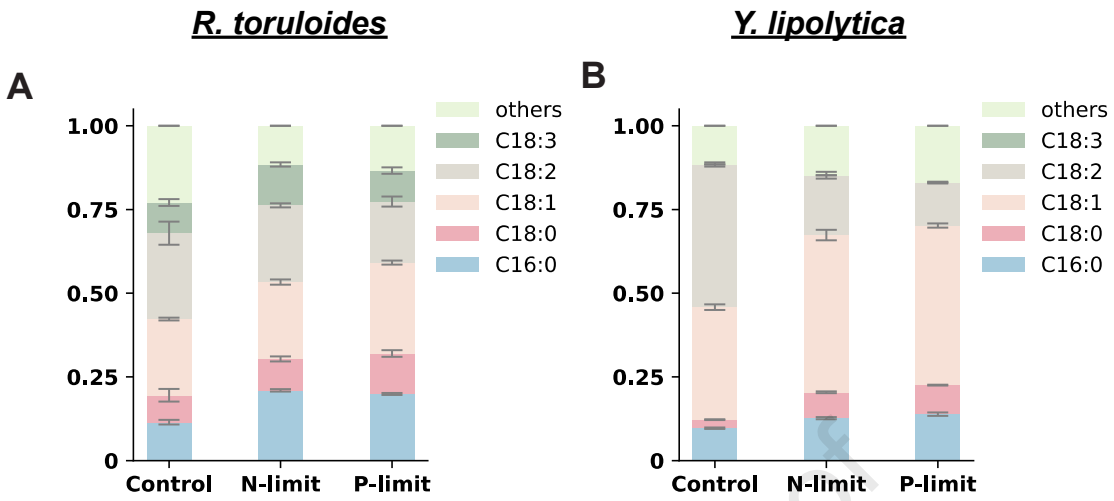

924 Fig. S4. Fatty acid composition (from saponification of whole cell lipids) changes modestly in
925 response to nutrient limitation, shifting towards more saturated fatty acid tails. (A) *R. toruloides*. (B)
926 *Y. lipolytica*. Mean ± *s.d.*, *n* = 3 biological replicates.
927

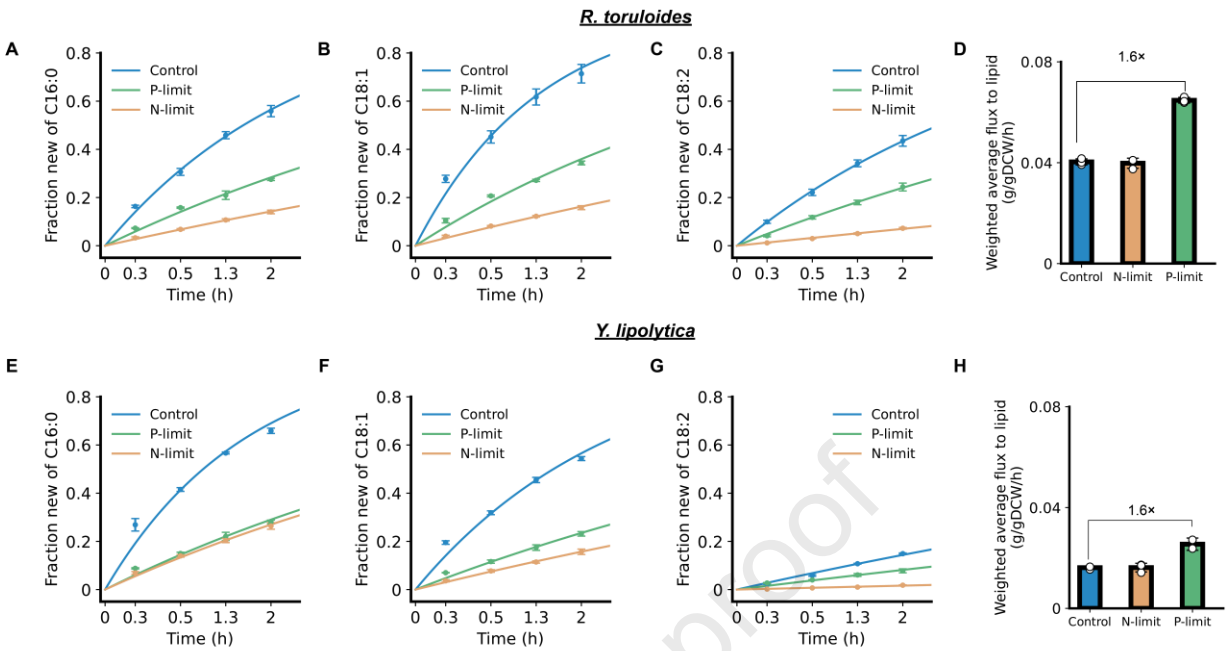

928

929 Fig. S5. Weighted average lipid biosynthetic flux based on 3 major fatty acids**.** Fatty acid labeling
930 kinetics of palmitate (A), oleate (B) and linoleate (C). (D) Synthetic flux to lipid biomass calculated
931 based on the weighted average of flux from the three fatty acids, derived by multiplying the
932 measured lipid pool size (Fig. 2B) by the weighted average of the exponential rate constant from
933 (A-C) (weighted based on measured abundance). (E – H). Same for *Y. lipolytica*. Mean ± *s.d.*, *n* =
934 3 biological replicates.

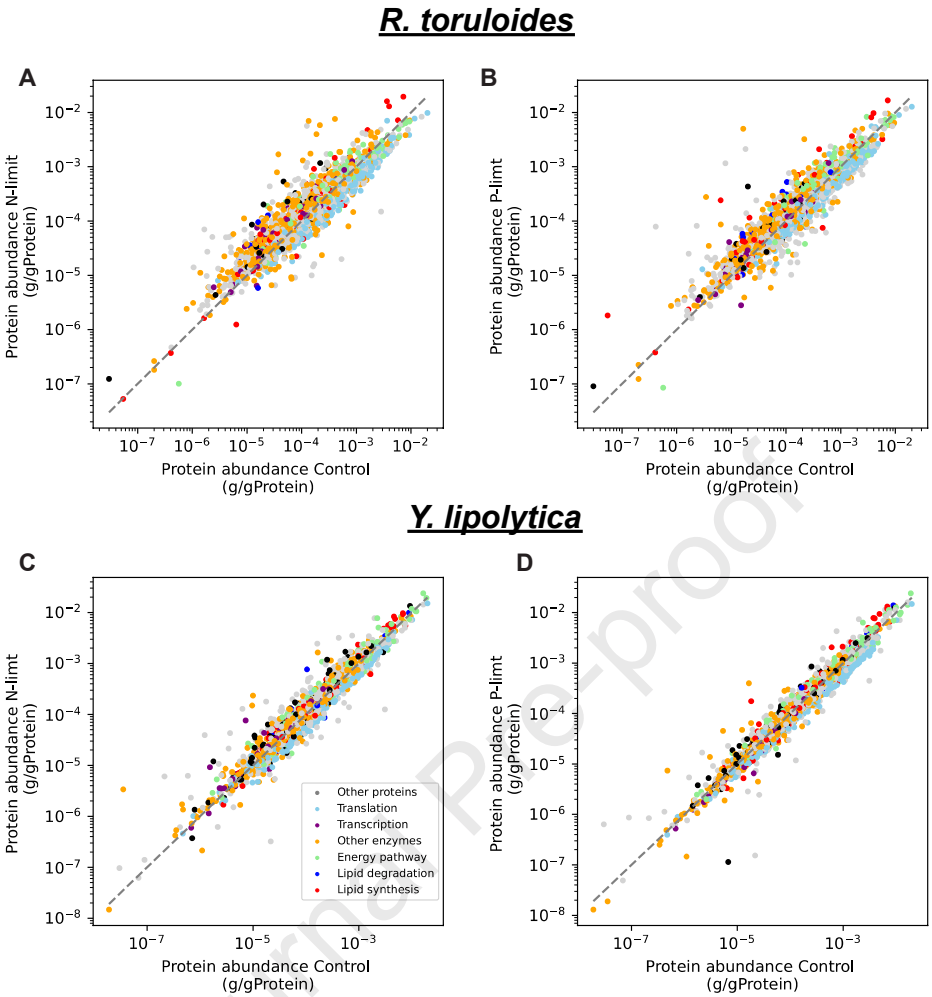

935 Fig. S6. Nutrient limitation rewires the proteome, decreasing translation machinery. (A) Individual
936 protein abundances (normalized to whole proteome) between nitrogen limitation and control *R.*
937 *toruloides*, with protein sector color-coded. (B) Same for phosphorus limitation and control. (C-D)
938 Same for *Y. lipolytica*. Each data point is the mean of $n = 3$ biological replicates.
939

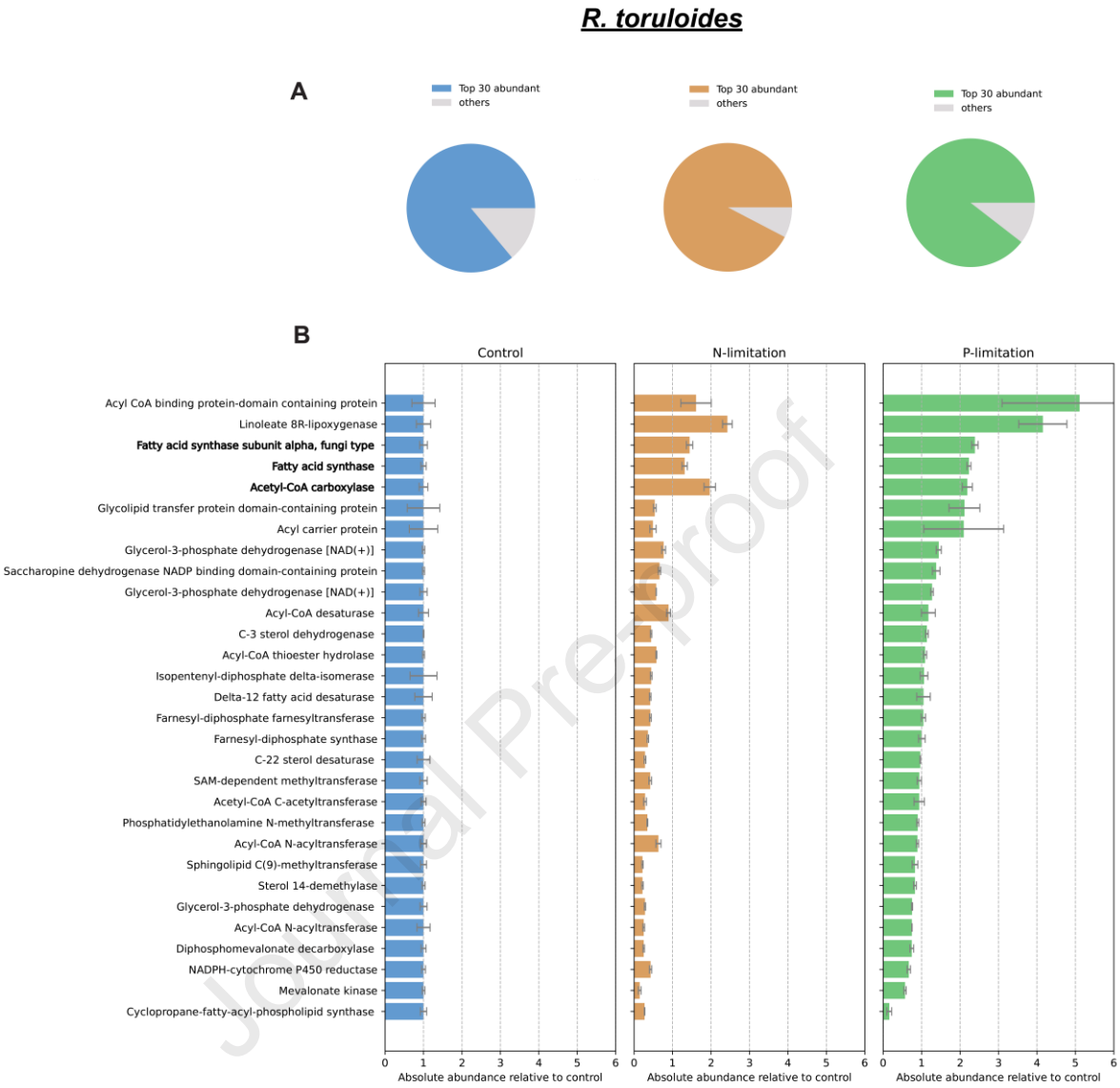

940 Fig. S7. Phosphorus limitation increases key lipid biosynthetic enzyme levels more nitrogen
941 limitation in *R. toruloides. (*A) Contribution of the 30 most abundant lipid biosynthetic enzymes to
942 the total lipid biosynthetic proteins, (B) Absolute protein abundance relative to control condition.
943 Mean ± *s.d.*, of *n* = 3 biological replicates

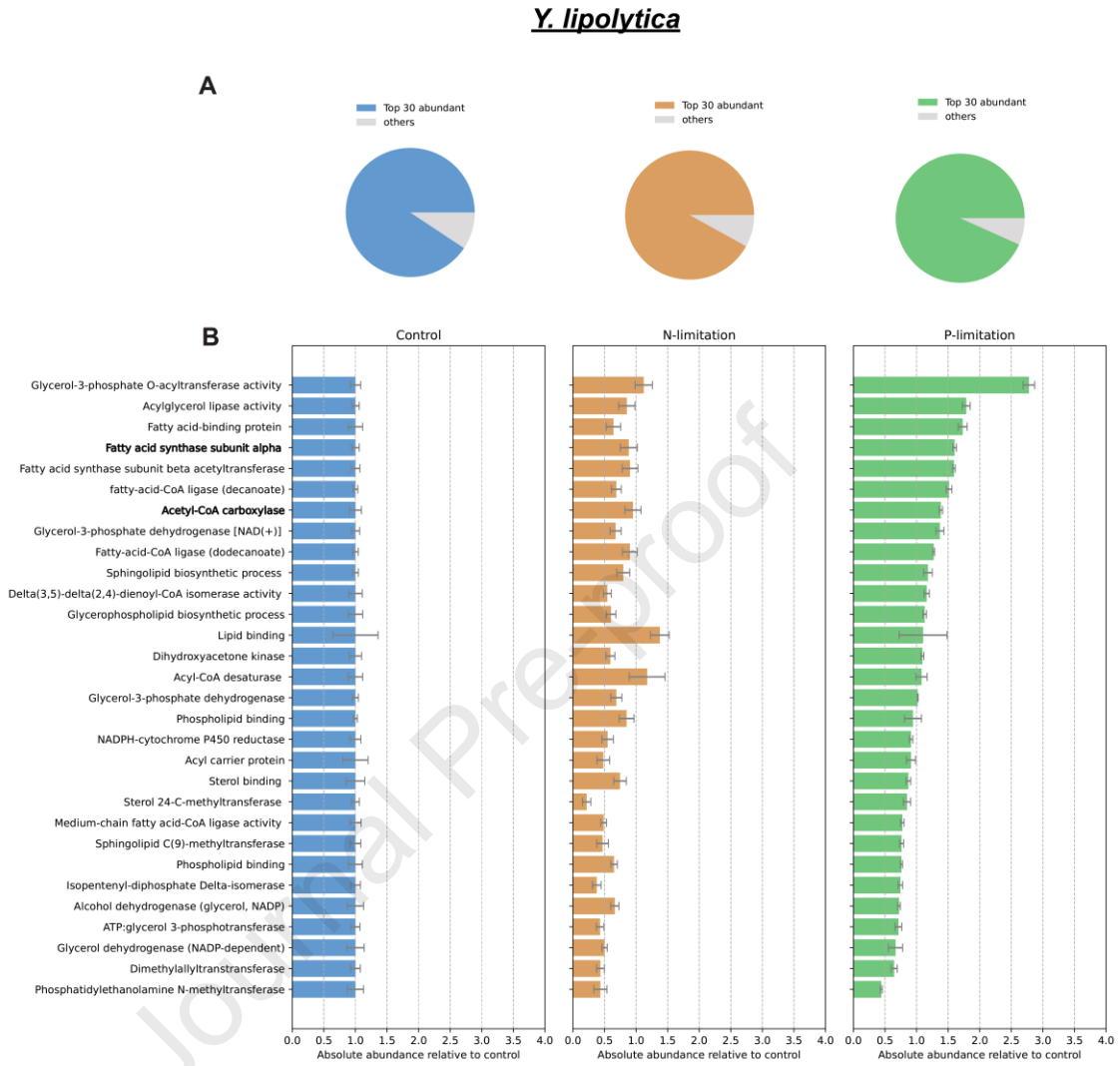

Fig. S8. Phosphorus limitation but not nitrogen limitation increases key lipid biosynthetic enzymes in Y. *lipolytica. (*A) Contribution of the 30 most abundant lipid biosynthetic enzymes to the total lipid biosynthetic proteins, (B) Absolute protein abundance relative to control condition. Mean ± *s.d.*, of *n* = 3 biological replicates

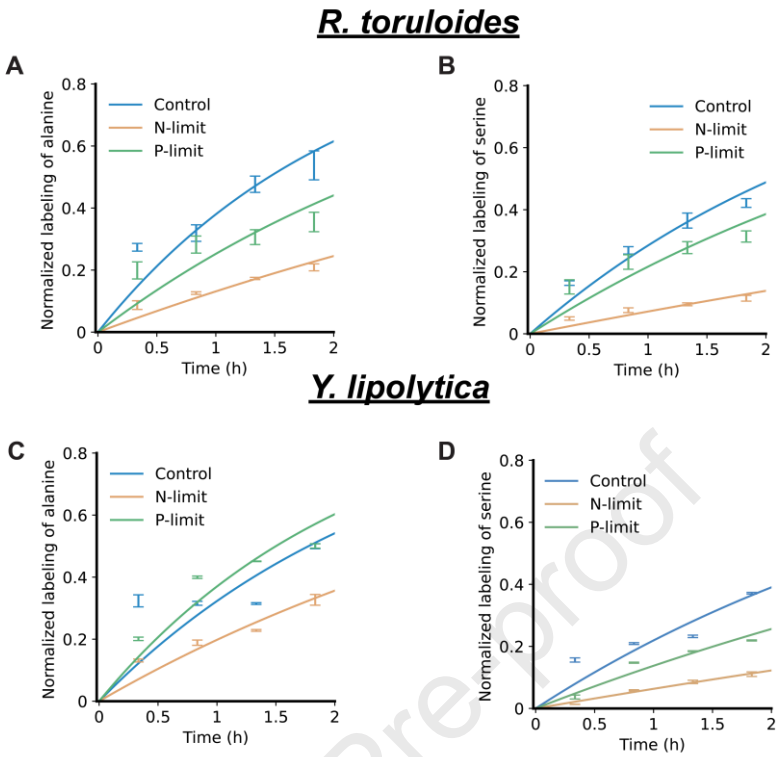

Fig. S9. Different amino acids show similar labeling kinetics. (A) Normalized labeling of alanine from hydrolyzed protein from freely growing or nutrient-limited *R. toruloides*. (B) Same for serine. (C-D) Same for *Y. lipolytica*. Mean ± *s.d.*, *n* = 3 biological replicates.

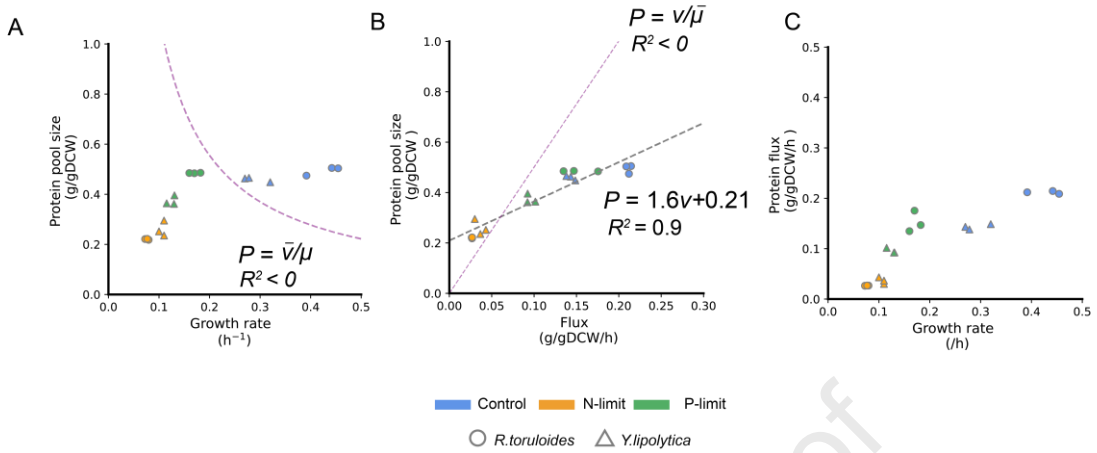

Fig. S10. Prediction of protein pool size with growth rate and protein synthetic rate. (A,B) Model prediction of the protein pool size using either (A) yeast growth rate and (B) protein synthesis flux as the variables. (C) Protein synthesis flux v.s. yeast growth rate. Symbols: v: flux, μ: growth rate. circle represents *R. toruloides* and triangulars represent *Y. lipolytica*. Color coding shows nutrient conditions. Data shown as mean from *n* = 3 biological replicates.

960

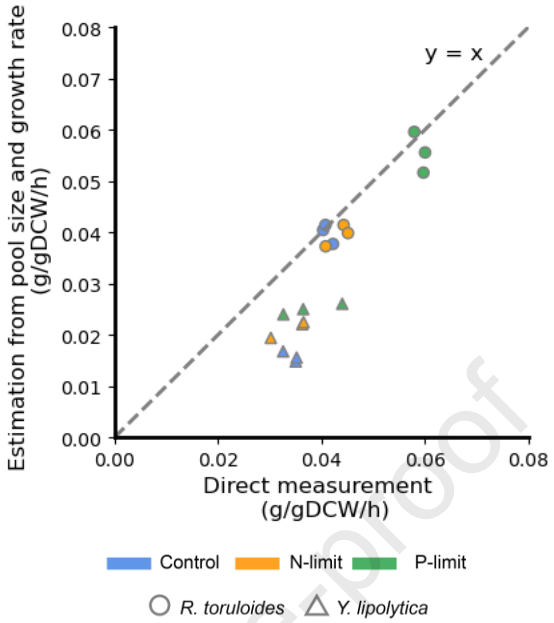

961 Fig. S11. Estimation of synthetic flux to lipid biomass based on growth rate and pool size generally
962 agrees with experimental measurements, but underestimates flux in *Y. lipolytica*, likely reflecting
963 fatty acid futile cycling in this species. Individual experimental data points are shown as circles for
964 *R. toruloides* and triangulars for *Y. lipolytica* with colors indicating the nutrient conditions.
965

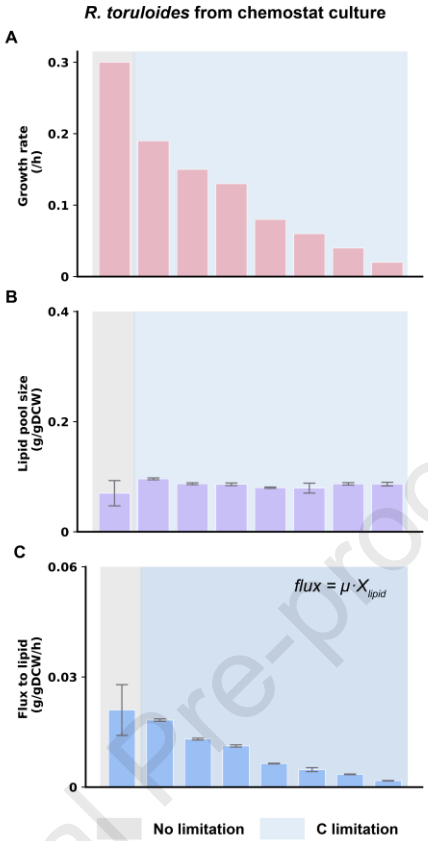

966 Fig. S12. Carbon (glucose) limitation in chemostats results in stable lipid pool size and decreased
967 lipid flux with slower growth rates. (A) Steady-state growth rate of *R. toruloides* AS 2.1389 strain
968 under no limitation, chemostat culture with glucose limitation of increasing stringency from left to
969 right, using published data from Shen *et al*. (Shen et al., 2013) (B) Associated lipid pool sizes. (C)
970 Calculated lipid biosynthetic flux, which is the product of growth rate from (A) and pool size from
971 (B).
972

973 Table S1. Media composition (per liter) for nutrient-replete (control) and limitation shake flask
974 culture.

media (g/L)	**Nutrient replete**	**N limitation (*R. t.*)**	**N limitation (*Y.l.*)**	**P limitation**
YNB (-) AA	6.7 g *			
YNB (-) AA (-) NH_4 (-) PO_4		0.7 g	0.7 g	0.7 g
$(NH_4)_2SO_4$	5 g from YNB	0.05 g	0.1 g	5 g
KH_2PO_4	1 g from YNB	1 g	1 g	0.01 g
KCl				0.542 g
Glucose	20 g *	5 g	5 g	5 g
C/N ratio (molar)		220	110	
C/P ratio (molar)				2262

975

976 * 6.7 g of YNB (-) AA contains the same sodium, calcium, magnesium and micronutrients as 0.7 g
977 of YNB (-) AA (-) NH4 (-) PO4. It further contains 5 g of $(NH_4)_2SO_4$ and 1 g of KH_2PO_4. For the
978 nutrient-replete media, glucose was added at 20 g/L unless otherwise indicated (experiments at 5
979 g/L glucose showed identical results).

980

Highlights

In N- or P-limited oleaginous yeasts, lipids accumulate without consistent flux rise

Lipid flux is measured directly via ^{13}C kinetic profiling

Math analysis validates the timescale assumption for flux analysis

N/P limitation shifts proteome—ribosomes down, lipid enzymes preserved